UPPSALA
UNIVERSITET

Modelling and Simulation of Electro-catalysts for Green Energy

From Solvated Complexes to Solid-Liquid Interfaces

JOSE LUIS LIMA DE JESUS SILVA

Abstract

In this thesis, I have worked with solid-liquid interfaces, adsorbed molecules on the surface, and solvated complexes using Density Functional Theory (DFT) calculations to find possible signatures that could help design suitable energy materials. More specifically, I have explored hybrid electrocatalysts for hydrogen evolution reaction (HER), XPS fingerprints of gas-phase melamine (monomer, dimer, trimer, and hexagonal packed arrangement), hexagonally packed melamine adsorbed on the Au(111) surface, and high-valence Ruthenium complexes along a reaction pathway in aqueous solution through a joint theory-experiment approach. First, I have explored single layer and hybrid-type systems as micro-reactors (current collector/catalysts) for HER with site-dependent calculations of the hydrogen binding free energy ΔG_H to estimate the HER activity, electronic structure, and Schottky Barrier Height (SBH) to measure the resistance for charge injection across the interface. Furthermore, we have predicted a new hybrid electrocatalyst Td-WTe$_2$/2H-MoS$_2$ employing DFT-based trends. Additionally, we have built carbon-based hybrid systems from a bilayer of g-C3N4 coupled with Td-WTe$_2$, 2H-MoS$_2$, and Graphene, and used an implicit solvation model to obtain more realistic signatures. The results show that g-C$_3$N$_4$/Td-WTe$_2$ has filled states in the Fermi level, which is a good indication of higher charge mobility. The SBH was evaluated with both GGA and HSE06, and Td-WTe$_2$/g-C$_3$N$_4$ has shown lower resistance for charge injection across the interface. Further, the induced dipole (driving force for electron injection) increases under higher hydrogen coverages, enhancing the catalytic activity. Finally, our results indicate that Td-WTe$_2$/g-C$_3$N$_4$ could be classified as an efficient electrocatalyst for HER. In the last two papers, we have estimated XPS finger-prints of molecular and solid-state systems by calculating the core-level binding energy shifts using the Janak-Slater transition state approximation. Also, we have developed a new methodology by combing DFT calculations with Monte Carlo Simulations using explicit solvation to resolve the XPS and understand the chemical shifts of the $[Ru^{II}\text{-}OH_2]^{2+}$ species, as well as of multiple PCET oxidation states. This work also shows that the chemical shift of $[Ru^{IV}=O]^{2+}$ is affected by the polarization of the explicit solvation model, and that we could only capture the experimental trend by using the complete first solvation shell and an XPS averaged spectra over a certain amount of snapshots from the Monte Carlo simulation. To the end, we also show that the nearest-neighbor potential contributions to the Ru 3d binding energies arising from atoms around the metallic center explain the higher 3d-state shifts of the oxo complex.

Jose Luis Lima de Jesus Silva, Department of Physics and Astronomy, Materials Theory, Box 516, Uppsala University, SE-751 20 Uppsala, Sweden.

This thesis is dedicated to my family

List of papers

This thesis is based on the following papers, which are referred to in the text by their Roman numerals.

I **Revealing the Contribution of Individual Factors to Hydrogen Evolution Reaction Catalytic Activity**
Yu Zhou, J. Luis Silva, John M. Woods, Joshua V. Pondick, Qingliang Feng, Zhixiu Liang, Wen Liu, Li Lin, Bingchen Deng, Barbara Brena, Fengnian Xia, Hailin Peng, Zhongfan Liu, Hailiang Wang, C. Moyses Araujo, Judy J. Cha
Advanced Materials, 30(18):1706076 (2018).

II **Unveiling the Interfacial Effects for Enhanced Hydrogen Evolution Reaction on MoS_2/WTe_2 Hybrid Structures**
Yu Zhou Joshua V. Pondick, J. Luis Silva, John M. Woods, David J. Hynek, Grace Matthews, Xin Shen, Qingliang Feng, Wen Liu, Zhixing Lu, Zhixiu Liang, Barbara Brena, Zhao Cai, Min Wu, Liying Jiao, Shu Hu Hailiang Wang, C. Moyses Araujo, Judy J. Cha
Small, 15, 1900078 (2019).

III **g-C_3N_4/WTe_2 Hybrid Electrocatalyst for Efficient Hydrogen Evolution Reaction**
J. Luis Silva , Barbara Brena, C. Moyses Araujo
J. **Phys. Chem. C, 124, 16, 8726-8735 (2020).**

IV **Spectroscopic Fingerprints of Intermolecular H-Bonding Interactions in Carbon Nitride Model Compounds**
Valeria Lanzilotto, J. Luis Silva, Teng Zhang Matus Stredansky, Cesare Grazioli, Konstantin Simonov, Erika Giangrisostomi, Ruslan Ovsyannikov, Monica De Simone, Marcello Coreno, C. Moyses Araujo, Barbara Brena and Carla Puglia.
Chemistry-A European Journal 24, no. 53: 14198-14206 (2018).

V **X-ray Photoelectron Fingerprints of High-Valence Ruthenium-Oxo Complexes along Oxidation Reaction Pathway in an Aqueous Environment**
J. Luis Silva, Isaak Unger, Tiago Araujo Matias, Leandro Rezende Franco, Giane Damas, Luciano T. Costa, Kalil C. F. Toledo, Tulio C. R.

Rocha, Arnaldo Naves de Brito, Clara-Magdalena Saak, Kaline Coutinho, Koiti Araki, Olle Björneholm, Barbara Brena and C. Moyses Araujo
J. Phys. Chem. Lett., 10, 24, 7636-7643 (2019).

Reprints were made with permission from the publishers.

Comments on my own contribution

I have contributed with the design of the atomic-scale models, calculations, written theoretical portions, and participated in the discussions for all the papers. For the joint theory-experiment **PAPER I** and **PAPER II**, I have performed the calculations and wrote contributions to the theoretical portion. For **PAPER III**, I have performed the calculations and took the leading on writing the paper. In **PAPER IV**, I have contributed to the XPS calculations, discussions, and theoretical portion. In **PAPER V**, I have participated in the design of the project, developed the theoretical methodology, responsible for the XPS calculations, participated in discussions, presentations of the project, and took the leading on writing the manuscript.

Additional Publications, not included in the thesis:

- **Hydrated electron generation by excitation of copper localized surface plasmon resonance.**
  Pavliuk MV, Gutierrez Alvarez S, Hattori Y, Messing ME, Czapla-Masztafiak J, Szlachetko J, Silva J. Luis, Araujo C. Moyses, A. Fernandes DL, Lu L, Kiely CJ.
  The Journal of Physical Chemistry Letters, 10(8), 1743-1749 (2019).

Contents

1. Introduction

The process of converting fossils extracted from the ground (i.e., crude oil with high concentrations of heavy oil) into chemicals and fuels (i.e., high valued oil), and the burning of fossil fuels has been negatively impacting the environment on a global scale. There is a considerable effort from the scientific community towards tackling energy challenges by focusing on developing new routes to improve the design of new catalysts that facilitate the synthesis of clean and renewable fuels. Hydrogen is among many possible candidates to address this issue since water is the only by-product of the reaction. Hydrogen can also be produced from electrochemical water splitting reactions, a valid route for large scale deployment. One of the bottlenecks is to achieve high efficiency to produce the H_2 fuel by using catalysts to minimize the overpotential that is necessary to drive the hydrogen evolution reaction (HER). Further, we need synergistic breakthroughs from theory and experiments to find an earth-abundant, stable, and low-cost alternative catalyst to drive the hydrogen evolution reaction (HER). In this section, I will introduce the primary motivations for this thesis.

1.1 Motivation and Thesis Outline

The severity of potential environmental issues caused by the increased concentration of greenhouse gases in the atmosphere, such as CO_2 is a continuous call for action from multiple sectors of society since most of the world's energy supply should instead reside on carbon-neutral sources. Despite many advances directed to sustainability, there is still a massive demand from society and multiple industrial sectors towards discovering potential friendly alternatives that might help future generations tackle the expected environmental crisis. Thus, scientific communities have been steadily working towards addressing energy challenges focused on developing new catalysts.

The sunlight energy that reaches the earth's surface in one hour is enough to power our planet for an entire year. Additionally, the most important mechanism to sustain life on our planet comes from photochemical processes to split the water into oxygen and hydrogen. Hydrogen is considered the most

promising energy carrier for driving transformations towards a renewable energy carrier economy [1]. It has additionally, clean combustion process with only water as the byproduct. Furthermore, hydrogen can be produced from electrochemical water splitting reactions, which is considered a potential cost-effective route for large scale spreading [2]. The hydrogen evolution reaction (HER) $(2H^+ + 2e^- \longrightarrow H_2)$ is a two-electron transfer mechanism that generates a catalytic intermediate and then H_2 fuel. The main challenge is to reach high energetic efficiency in this process by using catalysts to minimize the overpotential to drive HER. The scientific community has made significant progress towards Platinum (Pt) and noble-metals based catalysts for HER [3]. However, numerous disadvantages, such as high cost, scarcity, low selectivity, poor durability, toxicity, and environmental pollution issues, have constrained large scale applications. Hence, an earth-abundant, stable, and cost-effective alternative is yet on-demand, and additional synergistic breakthroughs in both theoretical and experimental approaches are still necessary. In general, chemical reactions controlled by catalysis can drive efficient energy conversions and facilitate the energy storage processes. Furthermore, electro-catalysts are fundamental to increase chemical reaction rates and control selectivity in fuel production. The design of catalysts for the splitting of H_2O into oxygen and hydrogen inspired by photosynthetic systems processes is a promising mechanism towards artificial energy conversion. From an electrochemical perspective, this reaction needs a reversible potential of 1.23 V at pH 1. Moreover, we can drive this reaction through the following two half-reactions: (i) oxidation of H_2O, and (ii) proton reduction to form hydrogen:

$$2H_2O \rightarrow O_2 + 4H^+ + 4H^- \qquad (1.1)$$

$$4H^+ + 4e^- \rightarrow 2H_2 \qquad (1.2)$$

$$2H_2O \rightarrow O_2 + 2H_2 \qquad (1.3)$$

If we linger to photosynthetic systems, the hydrogen released from the water splitting mechanism is stored in the carbohydrate $C_6H_{12}O_6$, as shown in the schematic diagram of Figure 1.1 (a), and following the chemical reaction:

$$6CO_2 + 12H_2O \rightarrow C_6H_{12}O_6 + 6O_2 + 6H_2O \qquad (1.4)$$
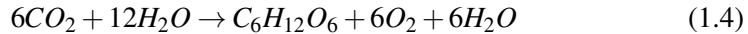
Hence, the carbohydrate production drives the storage of the hydrogen released from the water-splitting process. Additionally, the fundamental aspect of solar energy storage in photosynthesis relies on solving the bottleneck of the water splitting mechanism, a source of electron donors for the CO_2 reduction. However, the water oxidation is complicated as it involves multiple proton-coupled electron transfer (PCET) processes and the formation of intermediates species, leading to the O-O bonds [6]. In natural photosynthetic systems, the oxygen-evolving complex (OEC) such as the Mn_4CaO_5 cluster [7] activates the photo-driven process for water oxidation in Photosystem II (PSII) with the production of oxygen at a rate of 100-400 s^{-1} [8].
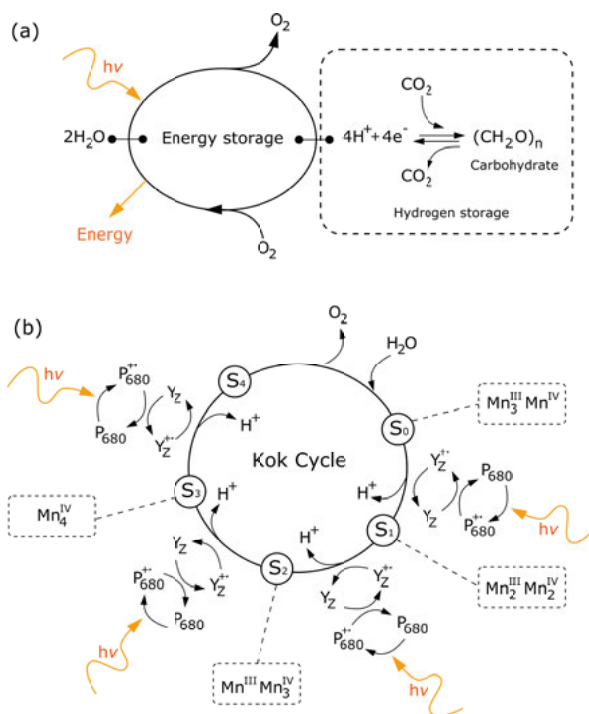
Figure 1.1. (a) Schematic diagram showing the storage of energy by photosynthesis to convert carbon dioxide into carbohydrates. (b) The Kok cycle diagram shows the absorption of photons by P680 to drive the splitting of water and the formation of O_2 after several Mn oxidation S-states of PSII-OEC. Y_Z represents the tyrosine which extracts the electron from the OEC to the highly oxidized P_{680} $^{+*}$. Adapted from [4, 5].

Figure 1.1 (b) shows a schematic diagram, also known as Kok Cycle, which represents the catalytic mechanism where OEC activates the oxidation of H_2O through several Mn oxidation states ($S_0 \rightarrow S_4$) to liberate O_2 [9, 10, 11, 4, 5]. Additionally, the sunlight-driven water oxidation represented by the PSII has the following procedure: (i) P_{680} absorb photons to form P_{680} *, (ii) P_{680} * oxidizes by transferring electrons to PS I and form high-valent oxidation state P_{680} $^{+*}$, (iii) P_{680} $^{+*}$ oxidizes tyrosine Y_Z to Y_Z^{+*}, (iv) Y_Z to Y_Z^{+*} extract electrons from the closest oxygen-evolving complex (OEC), and finally (v) the water is oxidized after four electrons are transferred through several Mn oxidation-states.

The first Ru-based catalytic systems for the oxidation of water was developed in 1985 by Meyer *et al.*, who synthesized the "blue dimer," which is composed by two oxo-bridged Ru(III) ([(bpy)$_2$(OH$_2$) RuORu (OH$_2$)(bpy)$_2$]$^{4+}$), and constitutes a mark in the development of water-splitting catalysts [12]. However, the successful application presents a low turnover number (TON)
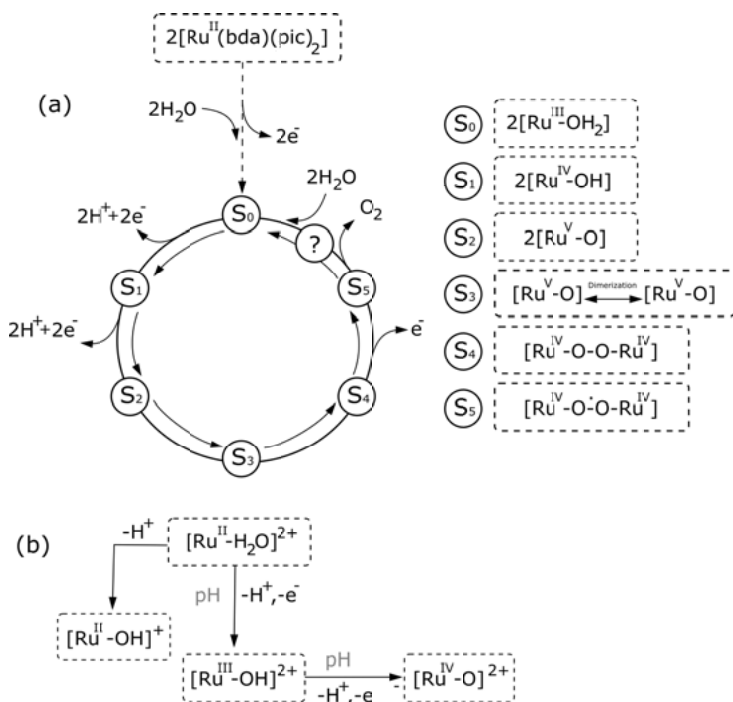
Figure 1.2. (a) Schematic water oxidation mechanism for Ru-based complex, and (b) Reaction pathway used in this work. Adapted from [29].

and turnover frequency (TOF) of 13 and 0.004 s^{-1}, respectively. These photosynthetic systems can be used as inspirations to help design prototypes for efficient fuel production. The reaction mechanisms proceed under high operational over-potentials, and the development of water oxidation catalysts (WOC) turns out to be essential to optimize the reaction rates. An optimal WOC should have low cost and toxicity, long-term durability and stability, and drive the reaction mechanisms at a high activity under low over-potentials. These efficient WOC are yet in demand for large scale deployment, since understanding the reaction mechanisms underlying WOCs is still a fundamental challenge. Recently, there has been much progress towards the development of transition metal complexes such as Mn [13], Co [14, 15, 16, 17, 18], Ir [19, 20, 21], Fe [22, 23], and Ru [24, 25, 26] with enhanced TONs (>100000)[26] and TOFs(>300 $s^{-}1$)[27]. The design of mononuclear Ru complexes by Duan *et al.* using axial ligands led to a considerable improvement of TOF values >1000 s^{-1} [27, 28]. The water oxidation induced by transition-metal catalysts leads to the formation of species with O-O bonds through two possible processes: (i) nucleophilic water attack on a metal oxo, and (ii) coupling of two metal oxo [30]. However, the O-O bonds are only formed after several oxidation reactions, and especially for Ru-based catalysts, the high reactivity of the intermediates RuIV=O and RuV=O are critical active species for

12

Figure 1.3. Hybrid 2D electrocatalyst model based on the structures g-C_3N_4/X (X = WTe_2, MoS_2 and Graphene).g-C_3N_4 is the catalyst and X represents the Current Collector.

this process. Duan *et al.* have illustrated a possible reaction pathway from a mononuclear Ru-complex ([RuII(bda(pic)$_2$] to generate the O-O bonds, as shown in Figure 1.2 (a) [26]. These intermediate Ru-based complexes are formed under different chemical environments, and they can be studied by a sensitivity technique such as X-ray photoelectron spectroscopy (XPS). The XPS is a powerful approach that allows one to extract high-resolution electronic structures for molecular species and solid-state systems in different chemical environments [31, 32]. The detection of these intermediates in the water environment needs sophisticated techniques such as X-ray photoelectron spectroscopy (XPS) with micro-jets at synchrotron facilities [33, 34]. Further, even for weak ligands such as those of Ru-based complexes, the micro-jet technique helps to avoid damaging the samples during the experiments. In **PAPER V**, we have studied the PCET reactions through the assessment of XPS from the model-system [RuII(bpy)$_2$(py)(OH$_2$)]$^{2+}$ (bpy = 2,2-bipyridine and py=pyridine) ([RuII-OH$_2$]$^{2+}$ for simplification) in the aqueous environment along a reaction pathway, as shown in Figure 1.2 (b). From the model-system, we have generated multiple high-valence Ruthenium complexes under different redox states and pH conditions. We have performed a sequential approach of Monte Carlo simulations [35, 36] and first-principles spectroscopy calculations to understand the experimental results and the underlying physics along the oxidation reaction pathway in an aqueous environment, focusing on understanding their physical-chemical properties.

New insights in the development of catalysts based on hybrid van der Waals heterostructures are also continuously empowered by experimental and theoretical approaches towards a more rational design [37, 38]. Furthermore, elec-

13

trocatalytic processes have shown to be influenced by multiple factors that are critical for the overall hydrogen production. The binding energy and differential Gibbs free energy for the adsorption of hydrogen has long been used as a potential descriptor to track new catalysts for HER [39, 40]. Additionally, the intra-layer charge transport and inter-layer charge injection have shown to affect and even modulate the overall HER efficiency [41]. Therefore, we have investigated multiple factors that interfere in the design of electrocatalysts through Density Functional Theory (DFT) calculations. Despite recent advances in the development of 2D transition metal dichalcogenides (TMDs) as catalysts for HER, we still need breakthroughs in both theory and experiment. In **PAPER I**, we have explored applications of DFT-based calculations for the semi-metallic Td-WTe_2 and semiconducting 2H-MoS_2 interfaces where Graphene and Au(111) are used as electrode contacts for HER. We have found unveiled the main factors controlling the catalytic activity for the semi-metallic system Td-WTe_2. As a direct consequence, we have extended the study to the hybrid structure 2H-MoS_2/Td-WTe_2 in **PAPER II**.

The exploration of carbon-based catalysts such as g-C_3N_4, and beyond metals remains a challenge [42]. The g-C_3N_4 is a porous metal-free polymer semiconductor that can be used for photo-driven production of hydrogen from water and as a potential catalyst for energy production [43, 44]. Therefore, in **PAPER IV**, we have explored the graphitic carbon nitride (g-C_3N_4) building block structures to understand how H-bonding interactions affect local electronic states and its respective functionalities. We have studied melamine molecules in gas-phase (Monomer, Dimer, Trimer, and Hexagonal packing) along with supported heterostructure composed by Au(111) and Melamine (hexagonal-packed). We have assessed the core level spectroscopy fingerprints using Density Functional Theory.

Additionally, in **PAPER III**, we have combined the g-C_3N_4 with the WTe_2, MoS_2, and Graphene, as hybrid 2D materials for efficient HER [45]. In the schematic Figure 1.3, we show a hybrid catalyst where the current collector (semi-metallic structure) is responsible for injecting charges into the primary catalyst g-C_3N_4 to enhance the HER. In this work, we have investigated solid-liquid interfaces by using an implicit solvation model to estimate the thermodynamic properties of the non-precious metal-based hybrid structures g-C_3N_4/X (X = WTe_2, MoS_2 and Graphene). The focus was on understanding the design of efficient catalysts for hydrogen evolution reaction (HER) through DFT-based properties such as (i) the free energy of hydrogen adsorption ΔG_H, (ii) Schottky barrier (iii) induced charge polarization. We have found that g-C_3N_4/WTe_2 is a potential outstanding electrocatalyst for efficient HER. In the next section, we will introduce the Density Functional Theory (DFT) approach, the theoretical framework used to support the simulations.

2. Computational Framework

In this section, we explore the theoretical framework of the many-body problem followed by the Density Functional Theory (DFT) approach, which is the theory used to support the simulations for the energy materials in this work. We explore the What, When, and How of tackling multiple instances of the modeling problem at the nanoscale.

2.1 Many-body Problem

Density Functional Theory (DFT) is a trendy framework and a straightforward choice for dealing with many-body problems in solid-state physics. Our primary focus is to find approximated solutions of the *Schrödinger* equation:

$$\hat{H}|\Psi\rangle = \mathrm{i}\frac{\partial}{\partial t}|\Psi\rangle. \tag{2.1}$$

for a non-relativistic Hamiltonian $\hat{H}$ represented by:

$$\hat{H} = -\frac{1}{2}\sum_{i=1}^{N}\nabla_i^2 - \sum_{\alpha=1}^{M}\frac{1}{2m_\alpha}\nabla_\alpha^2 - \sum_{i}\sum_{\alpha=1}^{M}\frac{Z_\alpha}{\left|\vec{r}_i - \vec{R}_\alpha\right|} + \frac{1}{2}\sum_{i=1}^{N}\sum_{j\neq i}^{N}\frac{1}{\left|\vec{r}_i - \vec{r}_j\right|}$$

$$+ \frac{1}{2}\sum_{\alpha=1}^{M}\sum_{\beta\neq\alpha}^{M}\frac{Z_\alpha Z_\beta}{\left|\vec{R}_\alpha - \vec{R}_\beta\right|} \tag{2.2}$$

The terms highlighted above represent the kinetic energy operators for N electrons and M nuclei, electron-nuclei, electron-electron, and inter-nuclear coulomb interactions, respectively, however, practical solutions of equation (2.1) are constrained by a large number of degrees of freedom from electrons (3N + N spins) and nuclei (3M). The first approach is to consider that electrons are much lighter than the nuclei, moves much faster than the nucleus and accommodates much faster than the nuclei to lower energy states under the influence of an external field, which means that the motion of the electrons and the motion of the nuclei can be separated (Born and Oppenheimer approximation)

[46]. For each nuclei configuration, the ground state solution can be approximated by solving the electronic form of *Schrödinger* equation:

$$\left[-\frac{1}{2} \sum_{i=1}^{N} \nabla_i^2 - \sum_{i=1}^{N} \sum_{\alpha=1}^{M} \frac{Z_\alpha}{\left| \vec{r}_i - \vec{R}_\alpha \right|} + \frac{1}{2} \sum_{i=1}^{N} \sum_{j \neq i}^{N} \frac{1}{\left| \vec{r}_i - \vec{r}_j \right|} \right] \tilde{\psi}_e(\{\vec{r}_i\}; \{\vec{R}_\alpha\})$$

$$= \varepsilon_e(\{\vec{R}_\alpha\}) \tilde{\psi}_e(\{\vec{r}_i\}; \{\vec{R}_\alpha\}) \tag{2.3}$$

where the electronic wavefunctions $\tilde{\psi}_e(\{\vec{r}_i\}; \{\vec{R}_\alpha\})$ depend parametrically on the nuclei configuration and must satisfy the time-independent equation. The first term of equation (2.3) is associated with kinetic energy, the second term represents an external potential, and the third term involves the complexity of repulsive electron-electron interactions. The next sections are focused on the Density Functional Theory (formulation of the many-body problem) as well as critical ground-state properties used in this work.

2.2 Density Functional Theory

Density Functional Theory (DFT) is a theory developed in the 1960s to circumvent the difficulties in solving the many-body problem, where the ground state total-energy is a functional of the electronic density $\rho(\mathbf{r})$. Hohenberg and Kohn [47, 48], which proposed that the functional of the total energy can be defined as:

$$\begin{aligned} E[\rho(\mathbf{r})] &= \langle \Psi | \hat{T} + \hat{V}_{ee} + V_{ext} | \Psi \rangle \\ &= F[\rho(\mathbf{r})] + \int d\mathbf{r}\, \rho(\mathbf{r})\, v_{ext}(\mathbf{r}) \end{aligned} \tag{2.4}$$

where the universal functional $F[\rho(\mathbf{r})]$ includes the kinetic energy and electron-electron repulsion term. The foundations of DFT relies on two important theorems developed by Hohenberg and Kohn, as follows:

1. (Uniqueness) $F[\rho(\mathbf{r})]$ is a functional of the electronic density $\rho(\mathbf{r})$ and the external potential $V_{ext}(\mathbf{r})$ is solely determined by the electronic density of the corresponding ground state with an additive constant.

2. (Variational Principle and Universality) Considering E_0 as the ground state energy for a system with N electrons under the effect of an external potential $V(\mathbf{r})$, the energy functional $E[\rho(\mathbf{r})]$ follows the variational principle so that $E[\rho(\mathbf{r})] \geq E_0$.

The first theorem establishes the one-to-one correspondence between the external potential and electronic density. From this theorem, any observable

can be written as a functional of the electronic density, which is the case for the total-energy. The second theorem establishes the variational principle and that the total-energy functional is universal. Therefore, for a system with $N = \int d\mathbf{r}\, \rho(\mathbf{r})$ electrons, the density $\rho(\mathbf{r})$ is represented on the ground state for a given external potential with a functional $F[\rho(\mathbf{r})] = \langle \Psi | \hat{F} | \Psi \rangle$ that is unique and well defined.

2.3 Kom-Sham formulation

The Hohenberg-Kohn theorems presented in the last section do not exhibit a formal expression of the functional $F[\rho(\mathbf{r})]$. However, Kohn and Sham [49] proposed the possibility of mapping a system with interacting electrons under the effect of an external potential V_{ext}. This mapping would take a fictitious system of non-interacting electrons with the same density $\rho(\mathbf{r})$ as for the interacting system and under the effect of an effective potential V_{eff}. According to the second theorem of Hohenberg-Kohn, the ground state density minimizes the energy functional, such that:

$$\delta E[\rho] = E[\rho + \delta\rho] - E[\rho] = 0 \tag{2.5}$$

For the interacting system, this restriction is included through a Lagrange multiplier term λ on the equation (2.5), such that:

$$\delta \langle \Psi | \hat{H} | \Psi \rangle = \delta \left[F[\rho(\mathbf{r})] + \int d\mathbf{r}\, v_{ext}(\mathbf{r})\rho(\mathbf{r}) - \lambda \left(\int d\mathbf{r}\, \rho(\mathbf{r}) - N \right) \right] = 0. \tag{2.6}$$

where $F[\rho(\mathbf{r})]$ is represented by:

$$F[\rho(\mathbf{r})] = T[\rho(\mathbf{r})] + E_H[\rho(\mathbf{r})] + E_{xc}[\rho(\mathbf{r})] \tag{2.7}$$

$T[\rho(\mathbf{r})]$ is the kinetic energy term, $E_{xc}[\rho(\mathbf{r})]$ represents the exchange-correlation energy factor [50] and the classical Coulomb potential $E_H[\rho(\mathbf{r})]$ can be written as:

$$E_H = \frac{1}{2} \int v_H\, \rho(\mathbf{r})\, d\mathbf{r} = \frac{1}{2} \int \int \frac{\rho(\mathbf{r})\, \rho(\mathbf{r}')}{|\mathbf{r} - \mathbf{r}'|}\, d\mathbf{r}'d\mathbf{r} \tag{2.8}$$

The derivative of equation (2.6) with respect to $\rho(\mathbf{r})$ can be expressed as:

$$\frac{\delta E}{\delta \rho(\mathbf{r})} = \frac{\delta T_s}{\delta \rho(\mathbf{r})} + \frac{\delta E_{xc}}{\delta \rho(\mathbf{r})} + v_{ext}(\mathbf{r}) + v_H(\mathbf{r}) - \lambda = 0 \tag{2.9}$$

Thus, we can obtain the Lagrange multiplier λ for the non-interacting system:

$$\lambda = \frac{\delta T_s}{\delta \rho(\mathbf{r})} + \frac{\delta E_{xc}}{\delta \rho(\mathbf{r})} + v_{ext}(\mathbf{r}) + v_H(\mathbf{r}) \tag{2.10}$$

such that the exchange-correlation potential $v_{xc}(\mathbf{r})$ is written as :

$$v_{xc}(\mathbf{r}) = \frac{\delta E_{xc}}{\delta \rho(\mathbf{r})} \tag{2.11}$$

Since the fictitious system is under effect of an effective potential $V_{eff}(\mathbf{r})$, the Hamiltonian can be defined as:

$$\hat{H}_{eff} = T'[\rho] + V_{eff} \tag{2.12}$$

By considering equation (2.5) for the non-interacting system, therefore:

$$\delta \langle \Psi | \hat{H}_{eff} | \Psi \rangle = \delta \left[T'[\rho(\mathrm{r})] + \int \mathrm{d}\mathbf{r} \; v_{eff}(\mathbf{r}) \rho(\mathbf{r}) - \lambda \left(\int \mathrm{d}\mathbf{r} \; \rho(\mathbf{r}) - N \right) \right] = 0 \tag{2.13}$$

such that the kinetic terms from the interacting and non-interacting systems are distinct ($T'[\rho] \neq T[\rho]$). The Lagrange multiplier associated with the non-interacting system can be expressed as:

$$\lambda = \frac{\delta T'[\rho(\mathbf{r})]}{\delta \rho(\mathbf{r})} + v_{eff}(\mathbf{r}) \tag{2.14}$$

Hence, the combination of equations (2.14) and (2.10) gives the effective potential:

$$v_{eff}(\mathbf{r}) = v_{ext}(\mathbf{r}) + v_H(\mathbf{r}) + v_{xc}(\mathbf{r}) \tag{2.15}$$

where the exchange-correlation potential $v_{eff}(\mathbf{r})$ involves the kinetic energy of both interacting and non-interacting systems along with a residual potential factor and can be rewritten as:

$$v_{xc}(\mathbf{r}) = \frac{\delta T[\rho(\mathbf{r})]}{\delta \rho(\mathbf{r})} - \frac{\delta T'[\rho(\mathbf{r})]}{\delta \rho(\mathbf{r})} + \frac{\delta E_{xc}[\rho(\mathbf{r})]}{\delta \rho(\mathbf{r})} = \frac{\delta E'_{xc}[\rho(\mathbf{r})]}{\delta \rho(\mathbf{r})} \tag{2.16}$$

However, the exact representation of the effective potential $v_{eff}(\mathbf{r})$ is unknown due to the exchange-correlation potential term $v_{xc}(\mathbf{r})$. The ground-state density of the non-interacting system can be found through the solution of N-one-electron *Schrödinger*-like equation:

$$\left[-\frac{1}{2}\nabla^2 + v_{eff}(\mathbf{r}) \right] \psi_i = \varepsilon_i \psi_i \tag{2.17}$$

The self-consistent solution of Kohn-Sham equation can be simplified as follows: (a) guess the electronic density $\rho(\mathbf{r})$ and use it to (b) calculate equations (2.15) and (2.16). The choice of the exchange-correlation functional is a primary factor because it can restrict the accuracy of calculated ground-state properties. Further, we use the effective potential v_{eff} estimated in (b) to solve equation (2.17) and find the Kohn-Sham orbitals ψ_i, which have no physical meaning. A new density can be estimated based on the mixing with the previous density. The process restarts from (b) until it reaches the convergence.

2.4 Exchange-Correlation Functionals

The accuracy of the ground-state properties obtained from the Kohn-Sham approach depends on the choice of the exchange-correlation functional. In this section, we provide details about possible approximations.

Kohn and Sham [47] initially proposed the Local Density Approximation (LDA). This functional depends only on the electronic density $\rho(\mathbf{r})$, which can be locally treated as the electronic density of a homogeneous electron gas. The exchange-correlation energy E_{xc}^{LDA} can be defined as:

$$E_{xc}^{LDA}[\rho(\mathbf{r})] = \int d\mathbf{r}\, \varepsilon_{xc}[\rho(\mathbf{r})]\, \rho(\mathbf{r}) \tag{2.18}$$

where $\varepsilon_{xc}[\rho(\mathbf{r})]$ represents the exchange-correlation energy per particle, where the density $\rho(\mathbf{r})$ at position $\mathbf{r}$ is considered as the density of a homogeneous electron gas. The term $\varepsilon_{xc}[\rho(\mathbf{r})]$ can be written as:

$$\varepsilon_{xc}[\rho(\mathbf{r})] = \varepsilon_x[\rho(\mathbf{r})] + \varepsilon_c[\rho(\mathbf{r})] \tag{2.19}$$

where $\varepsilon_c[\rho(\mathbf{r})]$ is a correlation factor and $\varepsilon_x[\rho(\mathbf{r})]$ represents the exchange contribution. Ceperley calculated the exchange-correlation energy for a homogeneous electron gas and Alder [51] using a Monte Carlo approach. Perdew and Zunger [52] suggested the most common parameterization of these exchange and correlation energies. The LDA approximation provides poor accuracy when applied to resolve heavily correlated systems and hinders the efficiency of describing hydrogen bonds [53]. LDA can also be extended to spin polarised systems referred to as the LSDA (local spin-density approximation) [54, 55].

We have used the Generalized Gradient Approximation (GGA) according to Perdew-Burke-Ernzerhof (PBE) [56] as the exchange-correlation functional, which depends on the electronic density and respective gradient of the electronic density, such that:

$$E_{xc}^{GGA} = \int d\mathbf{r} f(\rho(\mathbf{r}), \nabla\rho(\mathbf{r})) \tag{2.20}$$

It is essential to highlight that energy barriers from chemical reactions, among other properties, can be resolved with high accuracy [57, 58]. However, this functional underestimates the band gaps of semiconductors concerning experiments due to a strong delocalization of electrons. The use of hybrid functionals can help to tackle this issue. In **PAPER III**, we have used the hybrid functional HSE06 from Heyd, Scuresia, and Ernzerhof [59]. This functional includes the exact exchange-correlation functional PBE for short-range interactions with mixed approximations for the long-range interactions. These approximations are implemented in the Vienna Ab-initio Simulation Package (VASP) [60, 61].

2.5 Van der Waals interactions

When forming heterostructures, long-range intermolecular interactions, also known as Van der Waals (vdW) forces, become crucial factors to be taken into account. The source of these interactions might rely upon induced dipoles formed in the interface or instantaneously induced dipoles due to dispersion interactions (London Forces) [62]. These attractive forces are implicitly long-range interactions that cannot be treated appropriately by LDA or GGA. However, London interactions can be treated with the inclusion of an additive term in the total energy through different schemes such as DFT-D [63] and TS-vdW [64]. In our work, we have employed the method DFT-D3 developed by Grimme [65], which is an extension of the method DFT-D2 Grimme [66] where the total energy can be expressed by:

$$E = E_{GGA} - s_6 \sum_{i=1}^{N-1} \sum_{j \neq i}^{N} \frac{C_6^{ij}}{R_{ij}^6} F(R_{ij}) \qquad (2.21)$$

such that C_6^{ij} is a pair-dispersion coefficient, s_6 is a scaling factor, N represents the number of atoms, and R_{ij} is the distance between the atoms i and j. From equation (2.21), the damping parameter $F(R_{ij})$ is responsible for keeping the threshold for the long-range pattern:

$$F(R_{ij}) = \frac{1}{\left[1 + e^{a\left(\frac{R_{ij}}{R-1}\right)} \right]} \qquad (2.22)$$

where a represents the parameter of the model, and R represents the sum of the Van der Waals atomic radius $r_i + r_j$. The extension DFT-D3 includes the local environment by using self-consistent calculations to estimate the dispersion coefficient (geometry-dependent) and vdW cut-off radius.

2.6 Projector Augmented Wave (PAW)

The attributes of wave functions are peculiar in different regions of space. The interstitial region or bonding region is dominated by valence states and has smooth wave functions. However, regions near the nuclei have sharp features due to high-frequency oscillations. This factor maximizes the computational effort and numerical complexity to solve the Kohn-Sham equation. Therefore, it is necessary to decompose the wavefunctions into auxiliary smooth factors and contributions with rapid oscillations in small regions. The method PAW divides the space into an augmented region with spheres centered in the

atoms Ω_a [1] and an interstitial region Ω_i localized between the spheres. A linear transformation activated by the operator $\hat{T}$ transforms an auxiliary smooth wave function $|\tilde{\psi}_n\rangle$ into the Kohn-Sham wave-function $|\psi_n\rangle$:

$$|\psi_n\rangle = \hat{T}|\tilde{\psi}_n\rangle \tag{2.23}$$

Kohn-Sham equations can be rewritten as follows:

$$\hat{T}^\dagger \hat{H} \hat{T} |\tilde{\psi}_n\rangle = \varepsilon_n \hat{T}^\dagger \hat{T} |\tilde{\psi}_n\rangle \tag{2.24}$$

The linear operator $\hat{T}$ is chosen such that solving 2.24 leads to auxiliary smooth wave-functions. The operator $\hat{T}^\alpha$ is a linear transformation operator inside AE ($|\mathbf{r} - \mathbf{R}| < r_c{}^\alpha$) and can defined as:

$$\hat{T} = 1 + \sum_a \hat{T}^\alpha \tag{2.25}$$

The cutoff radius $r_c{}^\alpha$ is chosen, such that there is no superposition of spherical zones inside AE. Hence, smooth wave functions inside AE should be transformed into smooth partial waves $\tilde{\phi}_i^\alpha$, such that:

$$|\tilde{\psi}_n\rangle = \sum_i c_{ni}^\alpha |\tilde{\phi}_i^\alpha\rangle \tag{2.26}$$

where c_{ni}^α are expansion coefficients. Auxiliary partial waves ϕ_i^α are linear transformations of smooth partial waves $|\tilde{\phi}_i^\alpha\rangle$:

$$|\phi_i^\alpha\rangle = \hat{T}|\tilde{\phi}_i^\alpha\rangle = (1 + \hat{T}^\alpha)|\tilde{\phi}_i^\alpha\rangle \tag{2.27}$$

For external zones ($r > r_c^\alpha$) the linear operator $\hat{T}^\alpha$ vanishes:

$$\hat{T}^\alpha |\tilde{\phi}_i^\alpha\rangle = |\phi_i^\alpha\rangle - |\tilde{\phi}_i^\alpha\rangle = 0 \Rightarrow \phi^\alpha{}_i(\mathbf{r}) = \tilde{\phi}_i^\alpha(\mathbf{r}) , (r > r_c{}^\alpha) \tag{2.28}$$

and $\tilde{\phi}_i^\alpha(\mathbf{r}) = \langle \mathbf{r} | \tilde{\phi}_i^\alpha\rangle$ e $\phi_i^\alpha(\mathbf{r}) = \langle \mathbf{r}|\phi_i^\alpha\rangle$. Coming back to AE zones, $|\psi_n^\alpha\rangle = \hat{T}|\tilde{\psi}_n^\alpha\rangle$ should satisfy:

$$|\psi_n\rangle = \sum_i c_{ni}^\alpha \hat{T} |\tilde{\phi}_i^\alpha\rangle = \sum_i c_{ni}^\alpha |\phi_i^\alpha\rangle , |\mathbf{r} - \mathbf{R}^\alpha| < r_c{}^\alpha \tag{2.29}$$

where c_{ni}^α from equation (2.29) and (2.26) are identical. From a smooth projected wave function $|\tilde{p}_i^\alpha\rangle$ that satisfies the condition of orthonormality with the smooth partial waves in the region AE:

$$\langle \tilde{p}_i^\alpha | \tilde{\phi}_j^\alpha \rangle = \delta_{ij} \tag{2.30}$$

c_{ni}^α can be written as a linear functional of $|\tilde{\psi}_n^\alpha\rangle$:

$$\langle \tilde{p}_i^\alpha | \tilde{\psi}_n^\alpha \rangle = \sum c_{ni}^\alpha \delta_{i.j} = c_{ni}^\alpha \Rightarrow c_{ni}^\alpha = \int d\mathbf{r} \, \tilde{p}_i^\alpha(\mathbf{r} - \mathbf{R}^\alpha) \, \tilde{\psi}_n^\alpha \tag{2.31}$$

---

[1] Augmented Region

and smooth projection function must satisfy the completeness:

$$\sum_i |\tilde{\phi}_i^\alpha\rangle\langle\tilde{p}_i^\alpha| = 1 \qquad (2.32)$$

Therefore, the transformation operator inside AE zones can be expressed as:

$$\hat{T}^\alpha = \sum_i \hat{T}^\alpha |\tilde{\phi}_i^\alpha\rangle\langle\tilde{p}_i^\alpha| = \sum_i (|\phi_i^\alpha\rangle - |\tilde{\phi}_i^\alpha\rangle)\langle\tilde{p}_i^\alpha| \qquad (2.33)$$

$$\hat{T} = 1 + \sum_\alpha \sum_i (|\phi_i^\alpha\rangle - |\tilde{\phi}_i^\alpha\rangle)\langle\tilde{p}_i^\alpha| \qquad (2.34)$$

such that $\hat{T}^\alpha$ vanishes in regions outside the AE (2.28). Thus, the projection function $|\tilde{p}_i^\alpha\rangle$ is generated by several schemes [67]. Further, equation (2.34) and (2.23) allows us to calculate the Kohn-Sham wave-function $|\psi_n\rangle$ with the smooth partial functions centered on α atoms:

$$|\psi_n\rangle = (1 + \sum_\alpha \sum_i (|\phi_i^\alpha\rangle - |\tilde{\phi}_i^\alpha\rangle)\langle\tilde{p}_i^\alpha|) |\tilde{\psi}_n\rangle$$

$$= |\tilde{\psi}_n\rangle + \sum_\alpha \sum_i \langle\tilde{p}_i^\alpha|\tilde{\psi}_n\rangle|\phi_i^\alpha\rangle - \sum_\alpha \sum_i \langle\tilde{p}_i^\alpha|\tilde{\psi}_n\rangle|\tilde{\phi}_i^\alpha\rangle \qquad (2.35)$$

$|\tilde{\psi}_n\rangle$ can be obtained by solving equation (2.24). The wave function $|\psi_n\rangle$ that oscilates on Ω_a is described by pseudowavefunction $|\tilde{\psi}_n\rangle$. In this work we use PAW approximation implemented VASP.

2.7 Modeling the Solvation-Effect

In this thesis, we have studied solid/liquid interfaces using an implicit solvation approach by considering hybrid systems embedded in a water environment. The simulation of electrochemical systems in real conditions represents an incredibly complex task due to the high computational cost involved in handling explicit solvation effects. In order to efficiently describe the model of hybrid electrodes in contact with water for hydrogen evolution reaction (HER), we used VASPsol [68, 69] as implemented in the Vienna Ab-initio Simulation Package (VASP). This model describes the interface using the DFT benchmark, while the electrolyte is represented through an implicit solvation model based on the Poisson-Boltzmann equation, and the interface zone is a result of coupling the DFT and Poisson-Boltzmann equation electrostatically. The dielectric cavity is formed in the solvent by the solute, and the cavity can be built from the union of overlapping spheres centered in the solute atoms. The relative permittivity inside the cavity is that of a vacuum while taking the solvent's value outside this region. Further, the induced charges can be represented at

the cavity's surface. It is also possible to assume a continuous change of relative permittivity, which characterizes a diffuse dielectric factor. We have used this methodology in **PAPER III** to estimate the contribution of the solvation energy on HER.

2.8 X-Ray Photoelectron Spectroscopy Fingerprints

Core electrons, tightly bound to the atomic nuclei, are extremely sensitive to the atomic chemical environment. This fact is reflected in variations in the core electrons binding energies (BE), which can be measured by X-ray Photoelectron Spectroscopy (XPS) experiments. However, in complex molecular systems, a direct interpretation of the experimental results is often complicated, and the theoretical description is needed. The accurate measurement of BEs and its relaxed chemical environment effects was an outstanding achievement of K. Siegbahn *et al.* in 1957 recognized with the 1981 Nobel Prize in Physics. For molecules in the gas phase irradiated by X-rays with a particular frequency ν, the kinetic energy E_k of photo-emitted electrons can be measured. Hence, the BEs can be directly determined through the use of the photoelectric effect equation:

$$h\nu = E_B + E_k \tag{2.36}$$

However, for solids and surfaces, we need to add a factor (work function) to the equation (2.36), which represents the energy needed to take electrons from the Fermi level (FL) into the vacuum region, such that:

$$h\nu = E_B + E_k + \phi \tag{2.37}$$

where ϕ represents the work function. Figure 2.1 shows the X-ray irradiation mechanism where an excited electron moves from 1s energy level to the vacuum reference after breaking the energy defined by the work function ϕ. In applications of XPS measurements, usually, the BE differences (ΔBE) between two different states (chemical environments) are analysed with the vacuum or Fermi level taken as the reference. This quantity provides sensitive fingerprints from the local environment and bonding features from molecules such as melamine in gas-phase [70] (Monomer, Dimer, Trimer, and Hexagonal Packing) along with supported polymeric heterostructure grown on Au(111) as I have studied in **PAPER IV**, where the method also demonstrates the suitability to investigate surface phenomena. Further, it is also possible to use core-level shifts to observe *in situ* the evolution of heterogeneous catalytic reactions and study multiple reaction mechanisms. For example, by studying the ΔBE in **PAPER V**, we could show a fingerprint of the catalytically active specie RuIV oxo, which in turn could be used in other operando spectroscopy
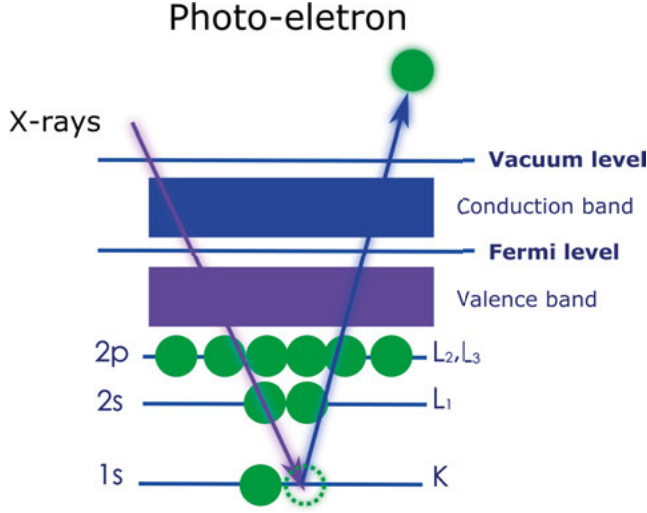
Figure 2.1. X-ray irradiation mechanism of 1s core level emission. The excited electron moves from 1s energy level to the vacuum region after breaking the threshold energy defined by the work function ϕ.

experiments to resolve the reaction pathways. It is usually standard practice to explore jointly theory-experiment approaches for a more critical assessment of physical properties associated with electronic structure and bonding of specific systems. The BE can be calculated through the difference between the final state relaxed with N-1 electrons and an initial and non-ionized state with N-electrons:

$$BE = E_F^{(N-1)} - E_I^{(N)} \tag{2.38}$$

However, it would be necessary to calculate the exact solution for the previously mentioned many-body problem by considering the initial and final states. In this thesis, we have used an alternative method implemented in VASP [72] and proposed by Janak and Slater as the transition state method (TS) [73, 71, 74, 75]. Figure 2.2 shows a schematic diagram representing the Initial State (IS) and Final State (FS), with excitation of one-electron from the core to the LUMO, and the Janak-Slater (JS) approach where half-electron is excited from the core-level to the LUMO. Additionally, we have the FS' (one electron excited from the core-level) and JS' (half-electron excited from the core-level) states, where we have ionized the slab by removing this excited electron. Hence, the final state is characterized by the extraction of the half-electron from the core level, considering the frozen core approximation under the PAW method to determine the partial occupancies. The JS transition state method is an "interpolating" approximation from the difference between the ground-state energies of the N and (N+1) particle systems. The approximation is obtained from partial derivatives of the Hohenberg-Kohn total energy (for
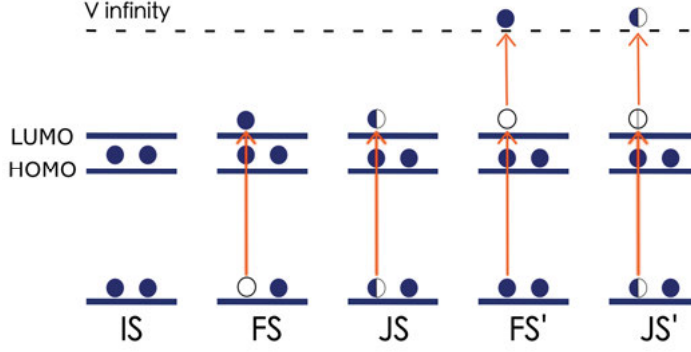
Figure 2.2. Diagram showing the Initial State (IS), Final State (FS), Janak-Slater (JS) approach where the half-electron is excited to the LUMO and both, FS' and JS' where the electron is removed from the LUMO to the vacuum. Adapted from [71].

partial occupancies) and evaluated halfway between two states, such that:

$$BE = E_{(N+1)} - E_{(N)} = \int_0^1 \varepsilon_i(\zeta_i)d\zeta_i \approx \varepsilon_i(\frac{1}{2}) \tag{2.39}$$

In this approach, Kohn-Sham eigenvalues (ε_i) are linear functions of the occupancy ζ_i and $\varepsilon(\frac{1}{2})$ is the half occupied core-level orbital energies. Hence, we provide the screening between the initial and final state core energy eigenvalues using only half-electron, where the BE can be approximated. We have considered the alignment of the core-level eigenvalues with the vacuum region, such that the binding energies are estimated as:

$$BE = <\phi_\infty> -\varepsilon_i(\frac{1}{2}) \tag{2.40}$$

and $<\phi_\infty>$ can represent the calculated electrostatic potential either along Z axis perpendicular to the surface (**PAPER IV**) or through the average along XYZ axis for molecules (**PAPER V**). This new approach considers the molecule centred in a large enough box with to avoid interaction between periodic images. Therefore, the electrostatic potential average over XYZ absorbs possible polarization effects of the molecule arising from multiple directions.

In **PAPER V**, we have studied the XPS fingerprints of Ru-based metallic centers from the model electrocatalyst, [RuII(bpy)$_2$(py)-(OH$_2$)]$^{2+}$, and its higher-valence ruthenium-oxo species. We have probed the Ru-based systems along a specific oxidation reaction pathway in the water environment by using the snapshots from a Monte Carlo simulation. The core-level binding energies can be represented by a linear combination of the potentials generated by the first coordination shell. The following equation is a generalized formulation

for the core-level binding energies considering the K-first-neighbors:

$$BE_{mc} = \beta_2 \, q_{mc} + \beta_1 \sum_{i=0}^{K} \frac{q_i}{r_{i,mc}} + \beta_0 \tag{2.41}$$

where q_{mc} is the formal charge on the metallic center atom (mc), q_i is the formal charge on neighboring atom i, and $r_{i,mc}$, its respective distance to the metallic center atom (bond length). Here, we have also explored a new approach to analyze the influence of potentials generated by the first neighbors of the model systems. The Bader Analysis [76, 77] was used to determine the formal charge for every single atom composing the first shell. The parameters of the model were obtained through ordinary least-squares (OLS) multi-regression, where BE represents the Ru 3d BEs shifts. The statistical treatment has shown to be significantly relevant, and further, this approach is capable of mapping intra-molecular positive and negative charge redistribution as a function of the formal oxidation state of a metallic center ion. This approach has shown its validity for analyzing XPS fingerprint profiles of catalytic reactions in the water environment.

2.9 Hydrogen Evolution Reaction (HER)

Electrocatalytic hydrogen evolution reaction (HER) is one of the most fundamental electrochemical reactions, and the scientific community has extensively studied it. The overall HER process in acidic media involves the use of electrocatalysts to drive the following reaction:

$$2H^+(aqueous) + 2e^- \longrightarrow H_2 \, (gas) \tag{2.42}$$
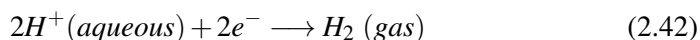
where for real systems, the reactivity will depend on variations of the electrostatic potential in the reference electrode. The HER can occur through two possible elementary reaction pathways, namely Volmer-Tafel or Volmer-Heyrovsky mechanisms. In both pathways, protons H^+ are adsorbed on the catalyst and reduced through the following reaction $H^+ + e^- + * \rightarrow H^*$, where * represents the adsorption site on the catalyst. Further, H_2 can be released through the Heyrovsky mechanism ($H^+ + H^* + e^- \rightarrow H_2$) due to the combination of solvated protons H^+ and hydride atoms H^- from the catalyst sites. The Volmer-Tafel process can also occur ($H^* + H^* \rightarrow H_2$), where two intermediate hydrogen atoms H^* coupled to the catalyst combine to form H_2 molecules. According to the Sabatier principle [78], the optimal catalyst should provide neither too strong nor too weak hydrogen binding strengths. This means that for the ideal catalyst, Gibbs free energy of the reaction $* + \frac{1}{2}H_2 \longrightarrow H^*$ at standard condition should be 0 eV. The differential Gibbs free energy is a central

concept to describe the thermodynamic equilibrium of HER processes, and it can be defined as:

$$\Delta G_{H^*} = \Delta E_{H^*} + \Delta E_{ZPE} + \Delta E_{Solv} - T\Delta S \quad (2.43)$$

where the adsorption of neutral hydrogen is undertaken on a specific surface site, ΔE_{Solv} represents the solvation effect, which can be estimated through the use of an implicit solvation model as implemented in VASPsol [79]. For the **PAPER I** and **PAPER II**, we did not consider possible solvation effects which means that $\Delta E_{Solv} = 0$. ΔE_{H^*} represents the differential adsorption energy of intermediate hydrogen adsorbed on the surface of the catalyst, as defined below:

$$\Delta E_{H^*} = \left(E_{nH^*} - E_{(n-1)H^*} - \frac{1}{2}E_{H_2} \right) \quad (2.44)$$

For $n \geq 1$, E_{nH^*} is the total energy with n hydrogens on the catalyst, $E_{(n-1)H^*}$ is the total energy of n-1 hydrogen coverage system and E_{H_2} is the gas phase energy of H_2. In equation (2.43), ΔE_{ZPE} represents differential zero point energy correction and it corresponds to the following expression :

$$\Delta E_{ZPE} = E_{ZPE}^{nH^*} - E_{ZPE}^{(n-1)H^*} - \frac{1}{2}E_{ZPE}^{H_2} \quad (2.45)$$

where $E_{ZPE}^{nH^*}$ and $E_{ZPE}^{(n-1)H^*}$ are the ZPE corrections for n and n-1 hydrogens adsorbed on the surface, respectively. $E_{ZPE}^{nH^*}$ represents the zero-point energy of H_2 in the gas phase and ΔS_{H^*} is the entropy difference between the adsorbed hydrogen and the gas phase which can be approximated as the entropy of H_2 gas at standard conditions [80], as follows :

$$\Delta S = (S_H - \frac{1}{2}S_{H_2}) \approx -\frac{1}{2}S_{H_2}^0 \quad (2.46)$$

We have performed estimations of the descriptor ΔG_{H^*} in **PAPER I,II**, and **III** by considering different conditions and hybrid heterostructures to understand the hydrogen evolution reaction better.

2.10 d-Band model

Since 1995, Norskov and Hammer formulated straightforward concepts [81], which are capable of predicting trends of heterogeneous catalytic reactions by considering changes in the adsorbate-substrate bond energy through the d-band model [82]. Since then, extensive studies were carried out to predict
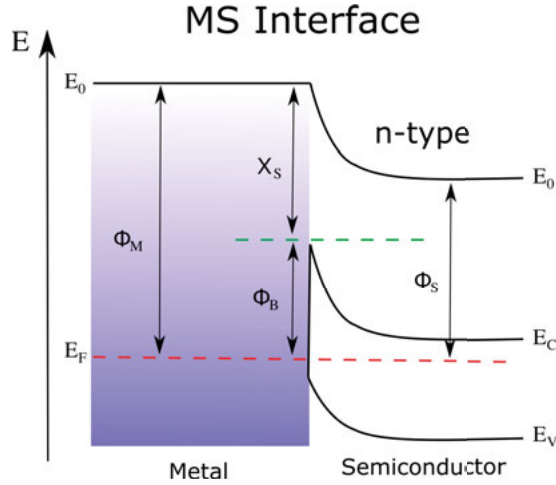
Figure 2.3. Scheme of the Schottky barrier (Φ_B) formed by the metal contacting a n-type semiconductor.

reactivity with particular trends arising from the electronic structure of pure metals bonded to ligands [83]. In the d-band model, the molecular adsorbate has fully occupied states that interact with fractions of filled states from the transition metals. As a consequence, the bond strength depends upon the filling states of the metal.

The adsorption of hydrogen in the metallic sites of the surface induces bonding and antibonding states above and below the Fermi level. The chemical bond strength can be tuned by the shift of the d-band center towards the Fermi Level. A downshift of the d-band might reduce antibonding states above the Fermi level and form weaker bond strengths between the adsorbate and substrate. In contrast, when the d-band center shifts upwards, the antibonding states are emptied above the Fermi level, and the bond becomes more potent. This model is applied in this work to analyze the bond strength between hydrogen and catalytic sites of different surfaces.

2.11 Schottky Barrier Height (SBH)

The formation mechanism and control of the Schottky Barrier Height (SBH) in metal-semiconductor (MS) interfaces is a challenging active research area in materials science [84]. The SBH is an essential feature for the development of electronic devices in the semiconductor industry, and multiple applications in nanotechnology. The MS interfaces have discontinuities of the energy levels responsible for the electronic conduction in each material. In the metal,

the electrical conduction depends on delocalized states around the Fermi level (FL), while the layer with the n-type semiconductor has electrical conduction derived from electrons close to the conduction band minimum (CBM). For hybrid systems composed of stacked 2D materials, the electric current flowing across the MS interface depends on the discontinuity of the electronic states between the layers. Therefore, the interlayer electronic transport across MS interfaces can be affected by the SBH, which can manifest as a potential energy barrier for the injection of charges to the semiconductor catalyst. Herein, we define the SBH as the difference between the CBM (projected DOS of the catalyst), and the FL.

Figure 2.3 shows a scheme of an interface between the metal and an n-type semiconductor, where Φ_B is the SBH (energy barrier for the flow of electrons from the metal to the semiconductor), E_C is the conduction band level, E_f the Fermi level (FL), Φ_M the metal work function, Φ_S the semiconductor work function and X_S represents the electron affinity of the semiconductor. In this thesis, we have investigated the SBH in **PAPER I, II** and **III** to better understand the resistance barrier energy for electron injection across the interfaces of hybrid 2D materials. Our main goal is to find a hybrid system where the height of the SB tends an optimal value (0 eV, or no SB) since this ohmic characteristic is an essential feature that provides reliable and fast charge injection for efficient reactions in the catalyst responsible for the HER activity.

3. 2D hybrid electroctalysts for hydrogen evolution reaction

In this section, we discuss **PAPER I** as we highlight how a synergy between theory and experiments can help improve the overall HER performance of nanodevices. During the HER process, the efficiency of charge injection across the interface and intra-layer charge transport might contribute to the catalytic activity. Hence, we proceed with **PAPER II**, where the influence of Schottky Barrier over vdW heterostructures built from stripes of MoS_2 and WTe_2 induces better HER performance. We concluded that the Schottky barrier quenches the HER activity on the catalyst, and multiple factors could contribute to the catalytic activity of hybrid vdW heterostructures. This work is an extension of the previous **PAPER I** as we combine MoS_2 (catalyst) and WTe_2 (metallic support) to improve the overall HER performance. Further, we present **PAPER III**, where we first introduce the interface effects of hybrid structures g-C_3N_4/X ($X = WTe_2$, MoS_2 and Graphene) that could help the design of efficient catalysts for HER. We have studied these hybrid catalysts using the following DFT-based properties: (i) the free energy of hydrogen adsorption ΔG_H, and (ii) Schottky barrier (iii) induced charge polarization. In this section, we will discuss what makes g-C_3N_4/WTe_2 a potential outstanding candidate as an electro-catalyst for efficient HER

3.1 Hybrid systems from MoS_2 and WTe_2: Revealing individual factors for hydrogen evolution reaction

MoS_2 is an earth-abundant layered solid, which belongs to the family of 2D semiconductors classified as dichalcogenides (TMDs). It has been highlighted as a promising candidate to substitute noble-metal based catalysts due to cost-effectiveness, thermodynamic stability, and high hydrogen evolution reaction rates, albeit limitations such as low electrical conductivity of inert Basal plane can impose limitations to the overall HER performance. Previous studies have shown that 2H-MoS_2 catalytic activity over the basal plane, can be boosted through induced vacancies, strain, and phase transformations [85]. Furthermore, the activation rate can also be enhanced through the hydrogenation of metallic edge sites and faster electron transfer rate (HET) over the inert
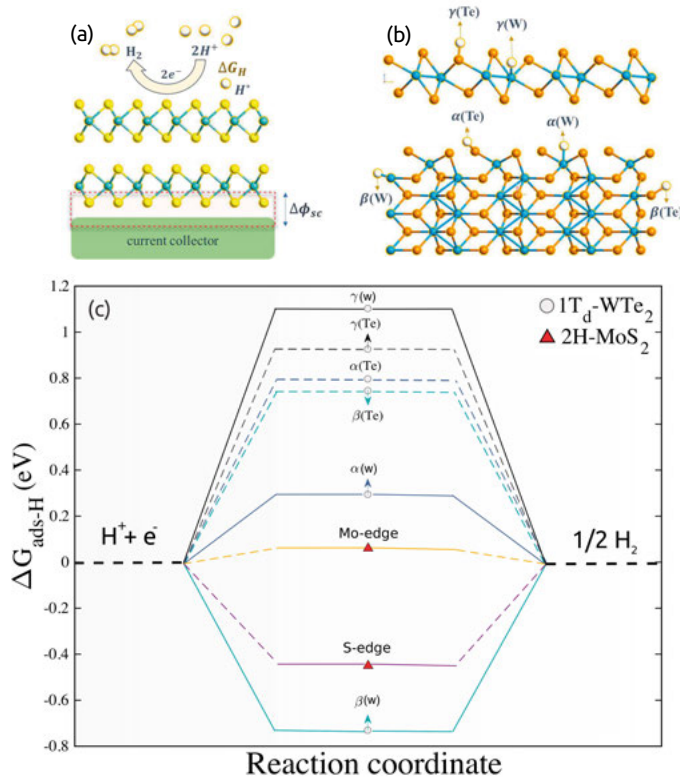
Figure 3.1. Key factors for hydrogen evolution reaction. (a) Schematic diagram of Heyrovsky and Tafel's reactions involved in hydrogen evolution reaction where ΔG_{H^*} represents the differential Gibbs free energy of hydrogen adsorption and $\Delta\phi_{SC}$ is the Schottky Barrier. (b) HER reactive sites for Td-WTe_2, where reaction sites (100) edge, (010) edge, and (001) basal plane are labeled as α, β and γ, respectively. (c) Comparison of ΔG_{H^*} between Td-WTe_2 and 2H-MoS_2 for various hydrogen-bonding sites. Adapted with permission from Yu Zhou, J. Luis Silva *et al.* [41] Copyright (2018) John Wiley and Sons.

basal plane [86, 87]. Unlike 2H-MoS_2 surface, mono-layer WTe_2 has structural stability under distorted Td phase and high electron mobility that allows fast transport of electrons towards reactive surface sites [88]. These latter attributes, along with multiple factors such as intra and inter-layer electron transport, interface coupling, Schottky Barrier, and differential free Gibbs energy (ΔG_{H^*}) for hydrogen adsorption can affect the overall HER performance of the system [41]. Figure 3.1 (a) shows a scheme of the HER process explained in section 2.9.

For hybrid vdW heterostructures, it is critically important to analyze the balance between the height of the Schottky Barrier ($\Delta\Phi_{SC}$), which is an indication of resistance to interlayer charge injection, and the thermodynamic
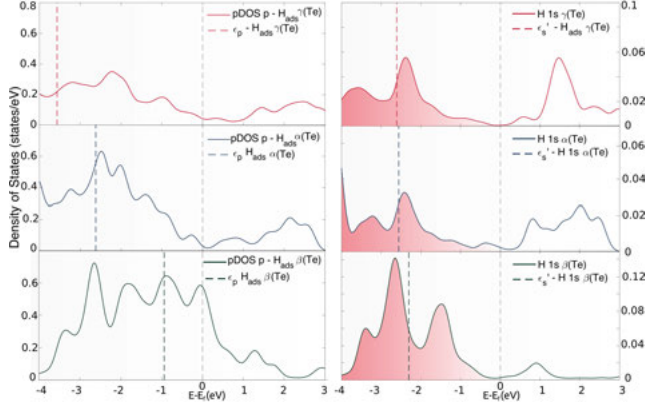
Figure 3.2. The p-orbital density of states sorted in descending order of ΔG_{H^*} from top to bottom. (left) the p-orbital density of states (filled lines) projected onto Te sites after the adsorption of hydrogen. Dashed lines indicate ε_p levels for p-orbitals and (right) s-Density of states projected onto adsorbed H atoms where $\varepsilon_{s'}$ is integrated over the interval [-4,0]. Adapted with permission from Yu Zhou, J. Luis Silva *et al.* [41] Copyright (2018) John Wiley and Sons.

descriptor ΔG_{H^*}. As mentioned before, for ideal catalysts, we should have $\Delta G_{H^*} = 0$ eV. The ΔG_{H^*} has been widely used as a potential descriptor to track efficiency for the HER activity on surfaces [89]. Therefore, we have calculated ΔG_{H^*} for a single layer Td-WTe_2, as shown in Figure 3.1 (c). Figure 3.1 (b) shows the schematic side and top views of Td-WTe_2 surface sites for the hydrogen adsorption. The comparison between ΔG_{H^*} from the inert basal plane of $2H - MoS_2$ ($\Delta G_{H^*} \approx 1.92$ eV) [29] and the edge planes of Td-WTe_2 (ΔG_{H^*} in the interval of $\approx$ [0.2-1.2] eV), as shown in Figure 3.1, indicates an improvement of the catalytic activity. The higher values ΔG_{H^*} for γ(W) compared to the other H-coverage indicates a weak interaction between H atoms and the basal plane site. The very negative ΔG_{H^*} associated with β(W) indicates a stronger bonding, which represents an obstacle to release H_2.

Additionally, Figure 3.1 (c) shows that ΔG_{H^*} varies significantly as a function of the adsorption site. Despite the high electron mobility of semi-metallic Td-WTe_2, the ΔG_{H^*} is unfavorable compared to the contrasting model $2H - MoS_2$ which has favorable ΔG_{H^*} but low electrical mobility. For Td-WTe_2, we can observe a slight improvement from $\gamma(W)$ downwards to $\alpha(W)$. In particular, $\alpha(W)$ has the potential to improve HER activity, and these predictions corroborate with the experimental results.

Hence, we unveil the electronic structure features that control the chemical bond strength and establish the structure-property relationship, as shown in Figures 3.2 and 3.3. The latter shows how the strength of the chemical bond correlates with the electronic structure of p and d-orbitals arising from
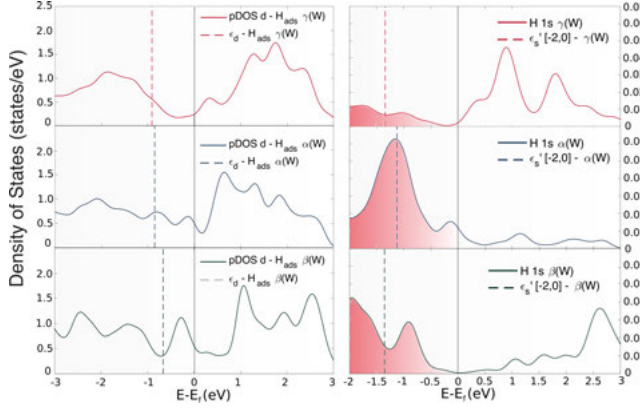
Figure 3.3. d-orbital pDOS sorted in descending order of ΔG_{H^*} from top to bottom. (left) d-orbital pDOS onto W-site (filled line) after adsorption of the hydrogen. (right) s-orbital pDOS. Adapted with permission from Yu Zhou, J. Luis Silva *et al.* [41] Copyright (2018) John Wiley and Sons.

metallic sites and s-orbitals from the adsorbed hydrogen. In particular, Figure 3.2 shows the p-orbital projected density of states (pDOS) (left) of γ(Te), α (Te) and β(Te) as well as the s-orbital pDOS from adsorbed H-atoms in each reactive site (right). It is important to highlight that for these cases, ΔG_{H^*} decreases from top to bottom. Figure 3.2 shows a strong overlap between p-orbitals from the surface site and s-orbitals from the hydrogen. The bond strength increases from the top γ(Te) to the bottom β(Te). The relative shift of single energy levels ε_p and $\varepsilon_{s'}$ towards ε_f show a stronger binding for β(Te) which favors ΔG_{H^*}. Figure 3.3 also highlights the bond strength considering the reactive tungsten sites after the adsorption of hydrogen. The slight shift of ε_d and $\varepsilon_{s'}$ towards the Fermi level also shows a stronger interaction between the s-orbitals from H-atom and resonant d-orbitals of the catalytic site.

In **PAPER I**, the HER activity was experimentally accessed for MoS_2 and WTe_2 with Gold as contact electrodes to understand possible factors that could influence the overall HER performance. We used DFT calculations for the following hybrid vdW heterostructures: Au(111)/ 2H-MoS_2 and Au(111)/ Td-WTe_2 (Details of calculations in **PAPER I**). Although the values of ΔG_{H^*} for MoS_2 (edge plane) should be more favorable, the experimental deployment of both edge and basal plane sites using Gold as a current collector did not show any HER activity. However, WTe_2 coupled with Gold as the current collector displayed HER activity, even though ΔG_{H^*} was estimated to be larger. In this case, an effective tuning of inter-layer charge injection ($\Delta\phi_{SC} = 0$) could be an essential step to boost the overall HER performance. Since larger $\Delta\phi_{SC}$ indicates a higher barrier for inter-layer charge injection, the WTe_2-gold interface does not provide any resistance. Figure 3.4 (a) shows a volcano plot

derived from the experimental measurements of the exchange current density (Y-axis) as a function of the ΔG_{H*} (X-axis) predicted from our calculations. This result highlights the fantastic synergy between the experiment and theory
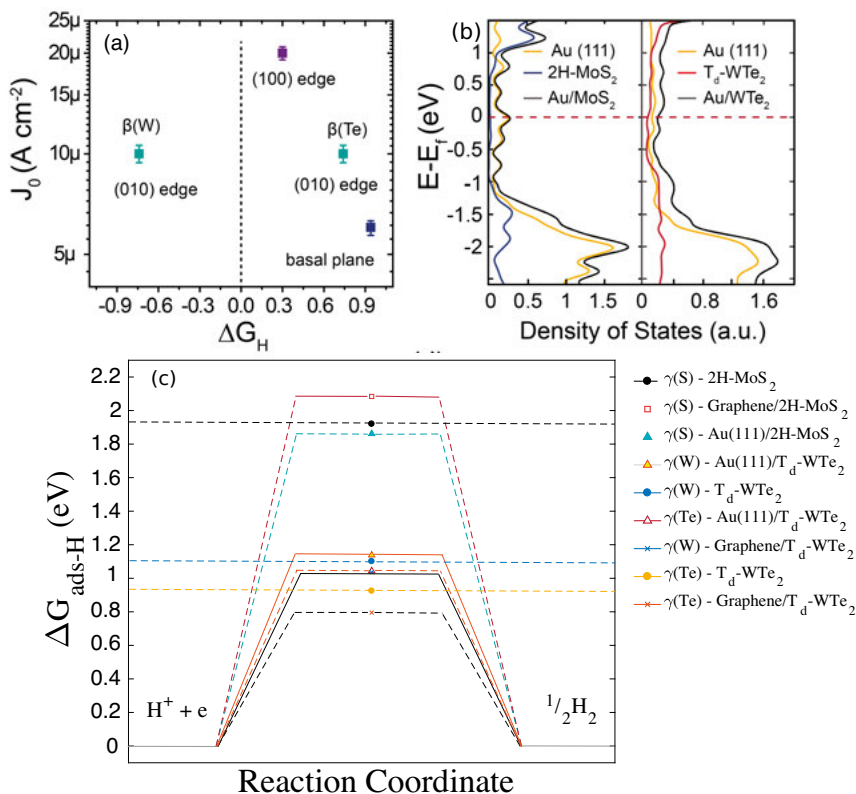

Figure 3.4. (a) A volcano plot of the exchange current density as a function of the calculated ΔG_{H*} for three different catalytic sites (b) Normalized projected density of states for Au(111)/2H-MoS_2 and Au(111)/Td-WTe_2 under less than 1% of average strain over Au(111) support. (c) Comparison of ΔG_{H*} values for the HER activity on the basal plane sites for the heterostructures. The yellow and cyan triangles represent the Au(111) supports coupled with 2H-MoS_2 and Td-WTe_2, respectively. The black cross indicates ΔG_{H*} for the Graphene/1Td-WTe_2 basal plane. An improved ΔG_{H*} was obtained for the basal plane sites of the Graphene/Td-WTe_2 heterostructure. Reprinted (adapted) with permission from Yu Zhou, J. Luis Silva *et al.* [41] Copyright (2018) John Wiley and Sons.

because the volcano shape was not necessarily expected. The importance of this contribution resides in the optimized design of catalysts since optimal catalysts should have ΔG_{H*} close to 0 eV and higher exchange current density. According to our predictions, the (100) edge is the most active plane for HER, and the basal plane the less active.

In Figure 3.4 (b) we plotted the calculated total and projected densities of states from Au(111)/2H-MoS_2 and Au(111)/Td-WTe_2 with estimated $\Delta\phi_{SC}$. Previous studies reported SBHs for Au(111)/2H-MoS_2 of approximately 0.88 eV and 0.763 eV with a mismatch of roughly 5.2% [90, 91]. Our results indicate an extremely low band occupancy with hybrid states around the Fermi-level for a very low mismatch of 0.81% and an approximate Schottky Barrier of 0.61 eV. Furthermore, Au(111)/Td-WTe_2 does not exhibit SB. A strong overlapping of states around the Fermi level shows ohmic-like contacting characteristic of the Au(111) /Td- WTe_2 interface, indicating an effective inter-layer injection of charges. Nevertheless, the analysis of SBH and thermodynamic alignment of ΔG_{H^*} can be crucial factors to improve HER performance. Within this purpose, Graphene was used as the current collector to tune HER activity of MoS_2 by reducing $\Delta\phi_{SC}$. Figure 3.4 (c) shows estimated ΔG_{H^*} for basal planes using graphene. A comparison of ΔG_{H^*} between monolayer 2H-MoS_2 and heterostructure Graphene/2H-MoS_2 indicates that the electronic properties are not critically affected even though experimental results indicate that heterostructure presents higher HER activity. The latter is an indication that intra-layer charge transport can restrict overall performance and become less efficient than inter-layer charge injection. Our ΔG_{H^*} also indicates an improvement of graphene- WTe_2 compared to Au-WTe_2, which is featured by experimental Tafel slopes of 92 and 141 mV dec^{-1}, respectively. However, WTe_2 and graphene-WTe_2 have shown similar overpotentials, which is indicative of efficient inter and intra-layer charge transport. Our calculations showed a better efficiency for the heterostructure. However, the experiment did not reproduce the previous results due to the size of WTe_2 nanoflakes and high charge mobility. These results provide a clear indicator that ΔG_{H^*} is not the only factor affecting the HER activity since the Schottky barrier $\Delta\phi_{SC}$ and charge mobility also modulates the overall HER performance.

3.2 Unveiling interface effects of hybrid MoS_2/WTe_2 for HER

We have previously shown that the high Schottky barrier could potentially suppress the electron transport between semiconducting and conducting support. Furthermore, the electronic structure and electron transport dynamics can be critically affected by the coupling of different supports, and the induced doping levels over MoS_2 could tune HER activity. Figure 3.5 (a) shows a schematic diagram of relative band edge alignment from a heterostructure constructed from a monolayer semiconductor 2H-MoS_2 and Td-WTe_2. The work functions of monolayer MoS_2 and WTe_2 are 4.36 and 4.5 eV, respectively. The relatively close Fermi level alignment between MoS_2 and WTe_2

leads to a lower Schottky barrier at the MoS_2/WTe_2 interface, smaller than the interface between MoS_2 and common metal electrodes. A lower Schottky barrier can improve HER activity by promoting efficient electron injection at the interface. We carried out DFT calculations to understand these improvements (calculation details in **PAPER II**). The calculated Schottky barrier heights are 0.25 eV for a 2H-MoS_2 monolayer on a Td-WTe_2 monolayer and 0.61 eV for a 2H-MoS_2 monolayer on Au (111) (Figure S1, Supporting Information of paper 2). Thus, the improved HER using the WTe_2 contact is due to a lower Schottky barrier between MoS_2 and WTe_2 compared to MoS_2 and gold. However, the additional improvement in HER for the heterostructure compared to the WTe_2 contact case cannot be explained solely by the SBH.
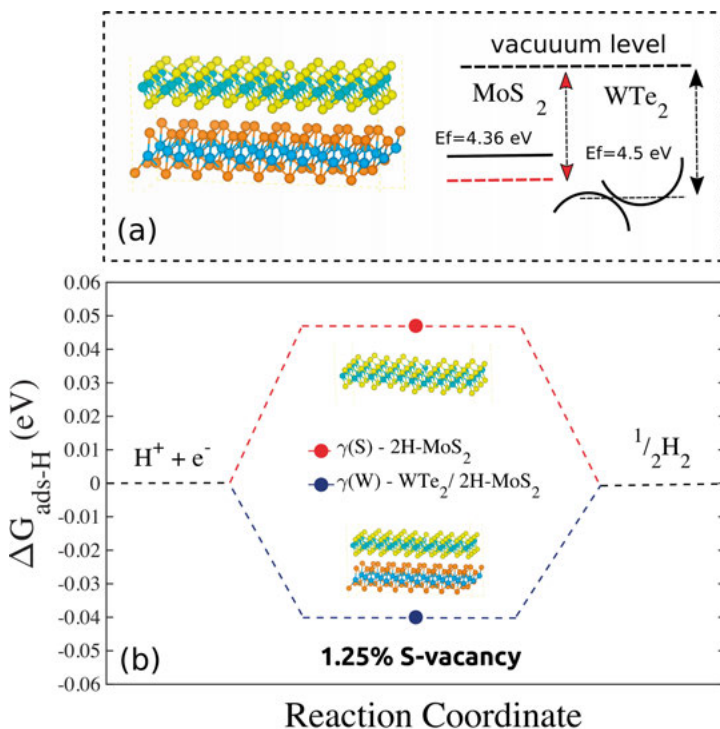
Figure 3.5. Interfacial effects on MoS_2/WTe_2. (a) Comparison of ΔG_{H^*} values for S-vacancy sites in the basal plane of the freestanding MoS2 monolayer (0.047 eV) and of the MoS_2/WTe_2 heterostructure (-0.040 eV). We assume one S-vacancy out of 80 S atoms for 1.25% vacancy concentration. Adapted with permission from Yu Zhou, Joshua V. Pondick, J. Luis Silva *et al.* [92] Copyright (2019) John Wiley and Sons.

Two main factors mentioned before contribute to improving the heterostructure's hydrogen evolution activity: change in ΔG_{H^*} of MoS_2 due to the underlying WTe_2 and enhanced charge injection due to the increased contact area of the interface and shorter electron transport length. However, it is essential

to highlight the possible experimental suppression of mirror charge formation since MoS_2 is coupled on semi-metallic WTe_2. First, we should consider the effect of ΔG_{H^*}. We have calculated only the basal plane ΔG_{H^*}. The measurements of HER activities were likely to have S-vacancies, which are catalytically active on the MoS_2 basal plane. For the calculated values of ΔG_{H^*} shown in Figure 3.5, we arbitrarily assumed an S-vacancy concentration of 1.25 in the MoS_2 monolayer.
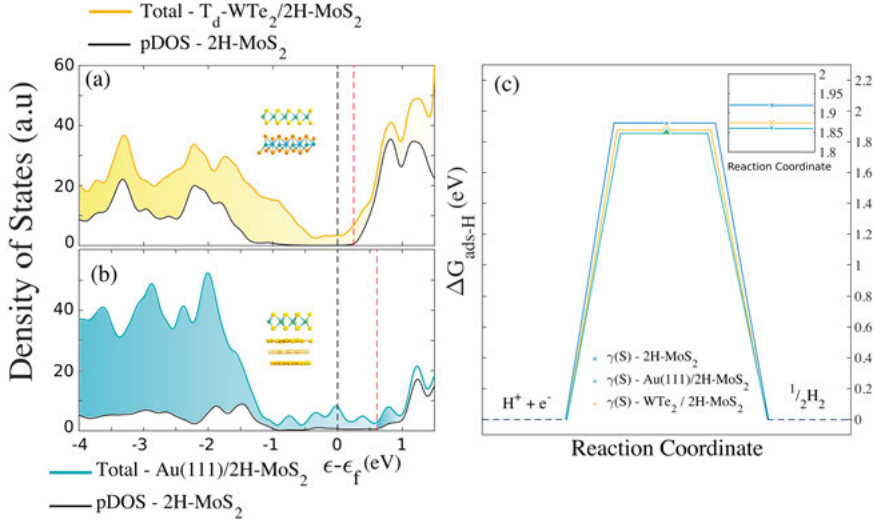

Figure 3.6. Calculation of $\Delta\Phi_{SC}$ for MoS_2/WTe_2 and MoS_2-gold interface. (a) Total DOS (yellow line) and projected DOS (black line) on the monolayer of 2H-MoS_2 in a Td-WTe_2/2H-MoS_2 heterostructure with a lattice mismatch of 2.3% - Calculated Schottky barrier of about 0.25 eV. (b) Total DOS (cyan line) and projected DOS (black line) on the monolayer of 2H-MoS_2 in a Au(111)/2H-MoS_2 structure with a lattice mismatch of less than 1% - Calculated Schottky barrier of about 0.61 eV. The red and black dashed vertical lines indicate the bottom of the conduction band and Fermi energy, respectively. Comparison of ΔG_{H^*} values for the intermediate hydrogen adsorption on sulfur sites in the basal plane of freestanding 2H-MoS_2 (blue), 2H-MoS_2 on Au (111) (cyan) and 2H-MoS_2 on Td-WTe_2 (yellow). A S-vacancy concentration of 0% is assumed for this calculation. Inset shows enlarged comparison of ΔG_{H^*} for the three different structures to show that the change in ΔG_{H^*} is negligible by interfacing MoS_2 with WTe_2. Adapted with permission from Yu Zhou, Joshua V. Pondick, J. Luis Silva *et al.* [92] Copyright (2019) John Wiley and Sons.

The comparison between freestanding MoS_2 monolayer and MoS_2/WTe_2 heterostructure using the same level of S-vacancies shows a very similar ΔG_{H^*} of 47 meV versus -40 meV, which results in ΔG_{H^*} not affecting the interface of MoS_2 with WTe_2. The ΔG_{H^*} for the cases without S-vacancies are trivial (Figure S2, Supporting Information in **PAPER II**).

As a second alternative explanation for the enhanced HER, we could possibly have a suppression of mirror charge formation by semi-metallic WTe_2. This comes from the fact that electrons are depleted from MoS_2 to reduce protons and form hydrogen. As a consequence, the remaining positive charge could be stabilized by the mirror charges from the substrate (SiO$_2$). The mirror charges can be suppressed by semi-metallic WTe_2 that couples directly to the monolayer MoS_2, and provide fast charge transport of electrons for high catalytic activity in the MoS_2 surface. Lastly, in the third hypothesis, MoS_2/WTe_2 heterostructure has a large contact area, which enhances the charge injection and reduces the electron pathway to the catalytic site.

To summarize, we have accessed the role of the hybrid structure MoS_2/WTe_2 interface through the calculation of DFT-based HER properties. The MoS_2/WTe_2 interface enhances the charge injection due to the Schottky barrier's small values, improved contact between the layers due to the large interface area, and reduced pathways for electron transport across the layer. Further, the hybrid structure MoS_2/WTe_2 was fabricated based on the results from the computational modeling and showed promising overpotential of 140 mV at 10 mA cm^{-2}, Tafel slope of 40 mV dec^{-1}, and prolonged stability. These results highlight the importance of interface design for HER catalysts.

3.3 g-C_3N_4 HER in water environment

As previously exposed, the combination of multiple factors such as intra and inter-layer charge transport can play a significant role in HER efficiency for stacked hybrid van der Waals structure [41]. Additionally, the effect of water is an essential element to be included in the DFT-based calculations of electrocatalysts. However, the specific treatment of solvation can be computationally expensive and considered as a bottleneck. Therefore, we have investigated the effects of solid-liquid interfaces employing Density Functional Theory using an implicit solvation model to estimate the ΔG_{H^*}. We have explored solid-liquid effects over bilayer of g-C_3N_4 coupled with stripes of Td-WTe_2, 2H-MoS_2, and Graphene through thermodynamic and electronic structure fingerprints where interface plays a significant role. Our results indicate that g-C_3N_4/Td-WTe_2 could outperform as an efficient electrocatalyst for hydrogen evolution reaction. We have chosen Carbon nitride g-C_3N_4 as the catalyst due to specific advantages such as stability[93], low ΔG_{H^*}, N-coordinated six-fold cavities from heptazine polymerization as well as C_3N_4 rings that contains anchoring catalytic sites for hydrogen evolution reaction [44, 94, 95]. These networks form layered structures under the effect of weak Van der Waals interaction forces. The HER activity of g-C_3N_4 (low-charge mobility) can be tuned using hybrid vdW heterostructures. This tuning results from the optimal
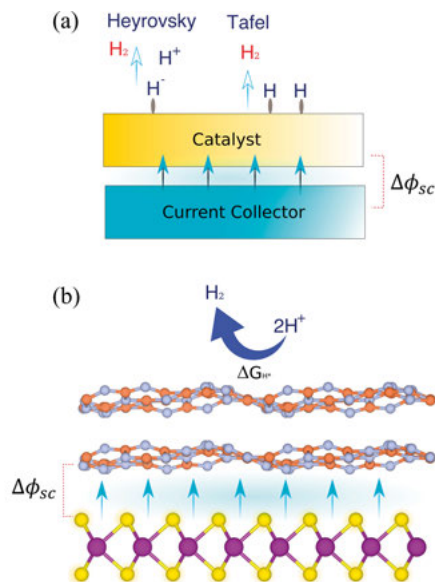
Figure 3.7. **(a)** Schematic diagram of Tafel and Heyrovsky reactions on nanodevice Catalyst/Current Collector where $\Delta\phi_{SC}$ represents the SBH. **(b)** Schematic structure g-C_3N_4/MoS_2. Reprinted with permission from J. Luis Silva *et al.* [45] Copyright (2020) American Chemical Society.

injection of electrons through the interface towards the catalyst's reactive sites. For hybrid electrocatalysts, built-in electric fields can be formed in the interface, and induce the transfer of electrons between the layers. Therefore, we are interested in optimal catalysts for HER in the electrode, where the hybrid structure also provides better charge injection.

The substrate is displayed on the bottom of the bi-layer g-C_3N_4, forming stacked vdW heterostructures, such as the ones shown in Figure 3.7 (a) and (b) where MoS_2 (substrate) and the bilayer g-C_3N_4 (catalyst) compose the hybrid structure. Figure 3.8 (a) shows a schematic diagram of the bilayer g-C_3N_4 as a function of H-atom coverage. The top layer contrasts with the transparent bottom layer and atoms in black, blue, and orange, respectively, represent hydrogen, nitrogen, and carbon. We have estimated the ΔG_{H*} for the red H-atoms in the top-view Figure 3.8 (a). For these configurations, Figure 3.8 (b) provides strong variations of ΔG_{H*} whether H-atoms are adsorbed on C or N sites for different hydrogen coverages. It means that local effects can interfere in the release of an intermediate H-atom (red color) from the porous region. The configurations σ_1, σ_2 and σ_3 represents the bilayer g-C_3N_4 with hydrogens coordinated to 3 Nitrogens in the porous region along with 1,2 and 3 H-atoms bonded to Carbon sites, respectively. As shown in Figure 3.8 (b) and Table 3.1, the ΔG_H varies significantly as a function of the probing site (C or N atoms),
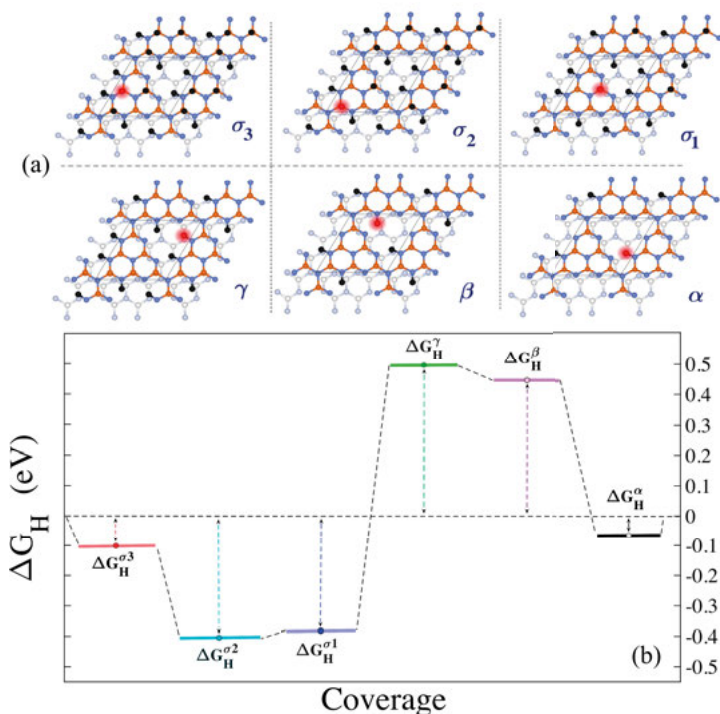
Figure 3.8. Bilayer g-C_3N_4 HER for different adsorption sites and coverages using implicit solvation model. **(a)** Schematic illustration of g-C_3N_4 sites where black dots represents the hydrogen which is adsorbed on the catalyst and red dots displays the hydrogen where ΔG_{H^*} was calculated. **(b)** ΔG_{H^*} for $\alpha, \beta, \gamma, \sigma_1, \sigma_2$ and σ_3 coverage including the solvation effect. Reprinted with permission from J. Luis Silva *et al.* [45] Copyright (2020) American Chemical Society.

Table 3.1. *Free energy of hydrogen adsorption ΔG_H for g-C_3N_4. Adapted with permission from J. Luis Silva et al. [45] Copyright (2020) American Chemical Society.*

H-Coverage	ΔG_H(eV)	ΔG_{H+Solv}(eV)
α	-0.17	-0.06
β	0.39	0.44
γ	0.53	0.49
σ_1	-0.38	-0.38
σ_2	-0.35	-0.40
σ_3	-0.14	-0.10

and hydrogen coverage of the catalyst. The descriptors $\Delta G_H^{\sigma_1}, \Delta G_H^{\sigma_2}$ and $\Delta G_H^{\sigma_3}$ shows that C-H bonds have strong bond strengths, as they exhibit sp^3-orbitals with small bond lengths of approximately 1.1 Å. The higher binding free energies of C sites could indicate easier adsorption (σ_1 and σ_2). Nevertheless, negative ΔG_H yields to difficulties in releasing hydrogen gas from the catalyst, which does not contribute to an efficient HER activity. Other factors as rippling effects from corrugated g-C_3N_4, strains, and doping could also impact

the HER activity [96]. As already mentioned before, g-C_3N_4 is optimal only for low hydrogen coverage. Additionally, we need higher overpotentials to induce the release of hydrogen in case of ΔG_{H^*} exhibiting high values. Our trends are in line with previous reports since we have found $\Delta G_{H^*} \approx$ -0.17 eV and 0.39 eV for $\theta =$1/3 and 2/3 without considering the implicit solvation model. However, the inclusion of the implicit solvation model is a promising approach and can be useful for modeling real devices, since electrocatalysts in real conditions are in a water environment. To summarize, ΔG_{H^*} shows a strong dependence on the probing site and hydrogen coverage. In the next section, we explore the combination of two hydrogens inside the porous region. This approach considers an average of β and γ to estimate ΔG_H. We will also explore possible interface effects of hybrid structures that could help with the design of efficient g-C_3N_4-based hybrid catalysts for HER.

3.4 Electronic Structure and Interface effects of g-C_3N_4/X ($X = WTe_2$, MoS_2 and Graphene)

Recently, g-C_3N_4/MoS_2 have shown low overpotentials for HER [97]. The DFT-based results show a considerable improvement of activity that depends on the strong coupling of vdW layers through Mo-N bonds that can facilitate hopping responses on the catalyst and charge injection across the interface towards the catalyst. We have coupled g-C_3N_4 bilayer with Graphene [98], 2H-MoS_2 [85] and Td-WTe_2 (distorted phase from 1H) [88], as shown in Figure 3.9 (a). These systems were coupled with g-C_3N_4 under mismatches of 2.34% (Graphene), 1.59% (2H-MoS_2) and 1.22% (Td-WTe_2). These materials have properties that might help to increase the efficiency of HER, such as high stability, high carrier mobility, and potential inter-layer charge transfer to the catalyst [98, 97, 92]. In Figure 3.9 (b), the ΔG_H of g-C_3N_4 is higher as compared to the hybrid structures. However, the averaged ΔG_H of the hybrid systems are very similar to each other. Therefore, the substrate could be equally affecting the performance of g-C_3N_4. The HER performance of catalysts in the solution can be affected by multiple factors such as interactions in the interface, temperature, and pH [99, 100, 101]. Although one could consider any of these hybrid heterostructures for deployment, and analysis of the SBH would still be necessary since the overall HER performance could depend on the charge injection across the interface.

In both Figures. 3.10 (a) and (b), we show the density of states (DOS) with projected DOS over g-C_3N_4 in blue. The Fermi Level and the conduction band minimum (CBM) are shown in black and red, respectively. We have estimated SBHs using the functionals HSE06 and GGA. As shown in Figure 3.10 (a) and
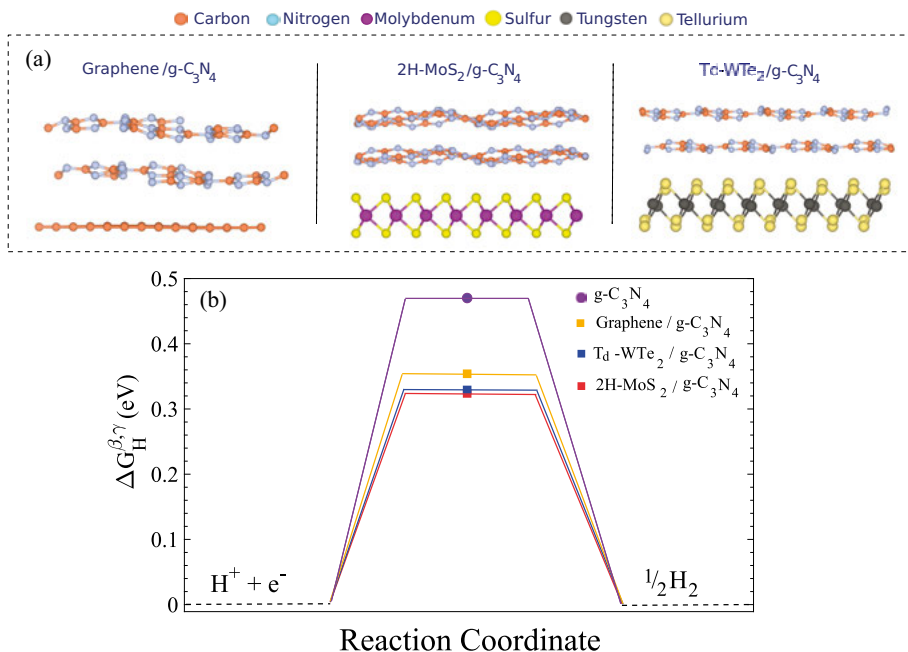
Figure 3.9. Perspective view of the heterostructures along with (a) HER descriptor for g-C_3N_4 coupled with Graphene, 2H-MoS_2 and Td-WTe_2 under $\theta = 1/3, 2/3$ and $3/3$ hydrogen coverage's inside the porous region. (b) Averaged ΔG_{H^*} over $\theta = 2/3$ and $3/3$ hydrogen coverage using the implicit solvation corrections. Reprinted with permission from J. Luis Silva *et al.* [45] Copyright (2020) American Chemical Society.

(b), the resistance to inter-layer charge injection is lower for Graphene/g-C_3N_4 dand higher for 2H-MoS_2/g-C_3N_4. For g-C_3N_4/Graphene, ΔG_{H^*} over γ and β in the porous region is significantly higher, and the total density of states has a gap that might constrain the charge mobility. However, the total density of states arising from hybrid g-C_3N_4/Td-WTe_2 has shown metallic characteristics. The evidence of metallic pattern showed by the projected DOS due to filled states in the Fermi level indicates higher charge mobility, possible fast redistribution of charges, and lower resistance to inter-layer electron injection across the interface. Therefore, g-C_3N_4/Td-WTe_2 could be considered as a potential candidate for HER since ΔG_{H^*} shows similarities to 2H-MoS_2/g-C_3N_4 and g-C_3N_4/Td-WTe_2 provides lower SBH. Additionally, hybrid systems such as metal-semiconductors might have an induced charge polarization along the interface [102].

The catalyst's hydrogenation can also induce the redistribution of charge density accumulation and depletion zones, affecting the injection of charges from WTe_2 to g-C_3N_4. We have estimated the charge accumulation and depletion zones for different hydrogen coverages of Td-$WTe2$/ g-C_3N_4. Addition-
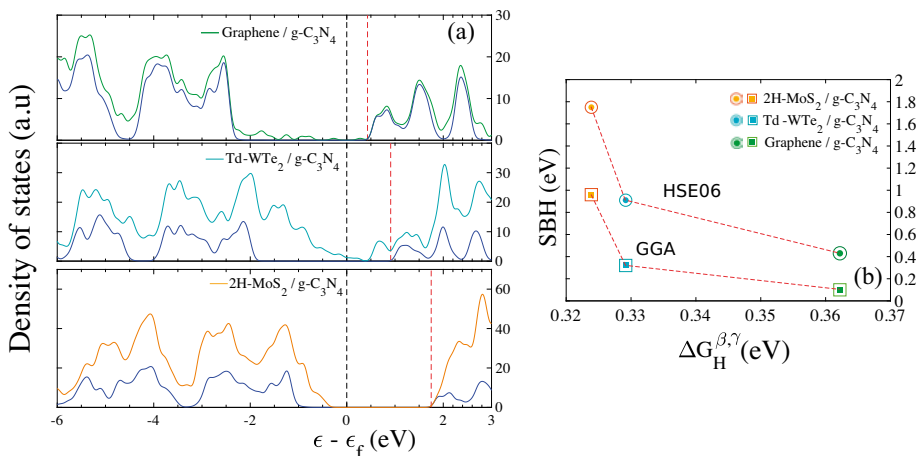
Figure 3.10. Total Density of States for g-C_3N_4/X with X= Graphene, WTe_2, and MoS_2 from top to bottom with black, green, cyan and purple lines, respectively. The blue area for each system represents the projected density of states over g-C_3N_4. The SBHs are estimated as the difference between the bottom of the conduction band (red line) and the Fermi Level of the metal (black line) using (a) HSE06. (b) SBHs vs. ΔG_{H*} inside the porous region for each hybrid system with the hybrid functional HSE06 (circle) and GGA (square). Reprinted with permission from J. Luis Silva *et al.* [45] Copyright (2020) American Chemical Society.

ally, we have also estimated the average induced charge density and dipole moments (perpendicular to the surface). Figure 3.11 (a) shows a normalized (yellow = 0, blue = 1) map of the charge density from Td-$WTe2$ / g-C_3N_4 perpendicular to the surface plane for Td-$WTe2$/ g-C_3N_4 without hydrogen. In Figure 3.11 (b), we show the bilayer g-C_3N_4 coupled with Td-$WTe2$ without hydrogens. The charge density accumulation (yellow) and depletion zones (cyan) from (b) show strong variations across the interface. Therefore, we have estimated the differential planar average charge density (Z-axis) for different hydrogenation states, as shown in Figure 3.11 (c). The purple, yellow, green and blue lines represents the bilayer Td-$WTe2$/ g-C_3N_4 with nH-atoms (n=0,1,2,3) in the catalyst, respectively. We can observe a strongly induced charge density redistribution along with the interface as long as we increase the number of H-atoms in the catalyst. The integration of these curves allows us to infer variations on the induced dipole across the interface. This dipole is a function of the number of hydrogen atoms in the catalyst. As shown in Figure 3.11 (d), the induced effects were integrated from Td-$WTe2$ up to the second layer of g-C_3N_4. However, we can observe minor effects when comparing the average induced dipoles integrated into different layers of g-C_3N_4. All the induced dipoles indicate a stronger driving force after the adsorption of more hydrogen. This driven force can induce an efficient charge injection across the interface. Therefore, direct channels for fast and robust charge in-
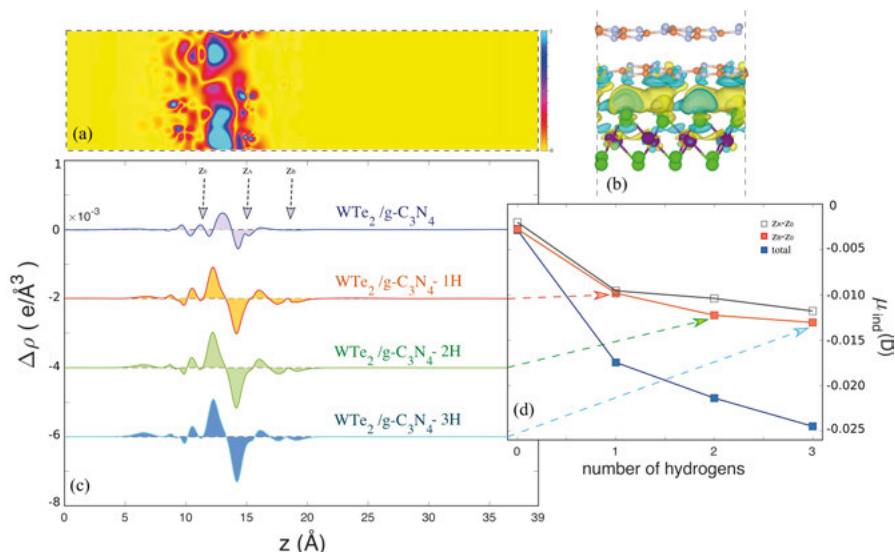
Figure 3.11. (a) Differential charge density color map normalized (yellow $= 0$, blue $= 1$) perpendicular to the surface plane of g-C_3N_4/$WTe2$ (b) Side view of g-C_3N_4/$WTe2$ with charge density accumulation (yellow) and depletion (cyan) zones (c) Planar average charge density varying the H coverage. Purple, yellow, green and blue lines represents bilayer g-C_3N_4/$WTe2$ with nH-atoms n=0,1,2,3 adsorbed in the catalyst, respectively. The curves are shifted by -n*0.002 in the Y-axis for better visualization (d) Interface induced dipoles as a function of the number of hydrogens and integrated from the interface $WTe2$ up to the first and second layer of g-C_3N_4. Reprinted with permission from J. Luis Silva *et al.* [45] Copyright (2020) American Chemical Society.

jection would provide electron-rich regions in the g-C_3N_4 catalyst for efficient HER.

The electronic structure fingerprints controlling the hydrogen binding energy, and the reaction activity were unknown for organic compounds like C_3N_4. We have resolved the H-N bonds and obtained fingerprints that correlate the electronic structure with the binding strength of the organic compounds present in the catalyst. The analysis is based on the partial DOS of MoS_2/g-C_3N_4 and Td-WTe_2/g-C_3N_4 for different hydrogen coverages (α, β and γ). Figure 3.12 (a),(b) and (c) shows the p-orbital projected density of states of N sites after the adsorption of H-atoms on Td-WTe_2/g-C_3N_4. The latter was plotted for the configurations γ, β, and α (descending from top-down). Additionally, Figure 3.12 (d),(e) and (f) also shows the projection of the s-orbitals (PDOs) from the hydrogen adsorbed on the Td-WTe_2/g-C_3N_4 surface. A significant result is that N-H bonds have strong s-p hybridization due to the filled states around the Fermi level (FL). Additionally, the assessment of ΔG_H in each specific N-site decreases as ε(center of the band) decreases towards
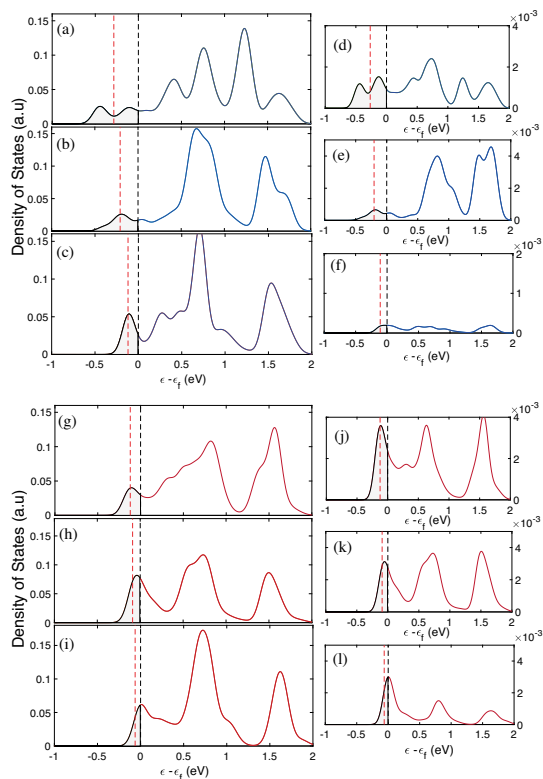
Figure 3.12. The pDOS for 1T-WTe_2/g-C_3N_4 under γ, β and α H-coverage for: N-sites (a), (b), (c) and adsorbed H-atoms (d),(e) and (f), respectively. Projected density of states for MoS_2/g-C_3N_4 under γ, β and α H-coverage for: N-sites (g), (h), (i) and adsorbed H-atoms (j),(k) and (l), respectively. The red dashed lines represents the center of the band integrated from -1.0 eV up to the Fermi Level. Dashed black line represents the Fermi Level and shaded area are filled states bellow the Fermi Level. The filled blue lines represents p-orbitals and red filled lines s-orbitals. Reprinted with permission from J. Luis Silva *et al.* [45] Copyright (2020) American Chemical Society.

FL. The previous result shows that the bond strength of the specific N-site is stronger if the center of the band is further away from the FL. The same trend is observed in Figure 3.12 (g),(h),(i),(j),(k) and (l) as ΔG_{H*} decreases according to Figure 3.9 (c). Thus, on-site projections of the density of states capture localized effects and provide a deeper understanding of the systems' binding strength and chemical properties. This work's importance relies on combining multiple factors that can support the design of efficient electrocatalysts for HER. We have also found strong evidence that supports the experimental deployment of g-C_3N_4/Td-WTe_2 as an efficient electrocatalyst for HER.

4. Spectroscopy properties of carbon nitride models

In this section, we will investigate the graphitic carbon nitride (g-C_3N_4) building block structures to understand how H-bonding interactions affect local electronic states. We have analyzed the melamine molecule in a vacuum (Monomer, Dimer, Trimer, and Hexagonal packing) along with the supported polymeric heterostructure Au(111) - Melamine (hexagonal-packed) employing a joint theory-experiment study of the X-ray Photoelectron Spectra of C 1s and N 1s.

4.1 Spectroscopic fingerprints of Carbon Nitride building blocks

The CN (Carbon nitride) sheets can derive from the most common building blocks such as either s-triazine or s-heptazine, as well as from Melamine (triamine-s-triazine) or Melem (triamine-s-heptazine). Recently, Lotsch *et al.* isolated crystalline phases of g-C_3N_4 [103, 104], where interconnected units of s-heptazine through -NH- bridges preserve $-NH_2$ amino groups. Figure 4.1 (c) shows a sketch of g-C_3N_4 with medium to strong hydrogen bonding interactions $-NH \cdots N = C$ forming zig-zag chains of packed 2D arrays. The g-C_3N_4 has also been previously experimentally observed as homogeneous networks of heptazine based on covalent -NH- bridges. The presence of hydrogen in g-C_3N_4 can be related to amino groups (NH_2) and bridging ($-NH-$) amines, and these hydrogen bonds can affect the core level binding energies. Since H-bonds can affect the photo-activity of g-C_3N_4, we have explored in detail the spectroscopic fingerprints of hydrogen interactions between $-NH_2$ functional groups and nitrogen atoms inside pyridine rings. [105, 106]. We have employed the JS transition state method, as described in the theory chapter, to calculate the C1s and N1s Core level shifts (CLS) of Melamine and we have tested the effect of different electron occupations, as shown in Figure 4.2. We have performed the calculations to estimate the final state effect for the neutral and charged Gas-Phase of Melamine. Figure 4.2 shows a better agreement between theory and experiment for the half-core hole approach. The molecules were centered inside a supercell with the vacuum in all directions to avoid
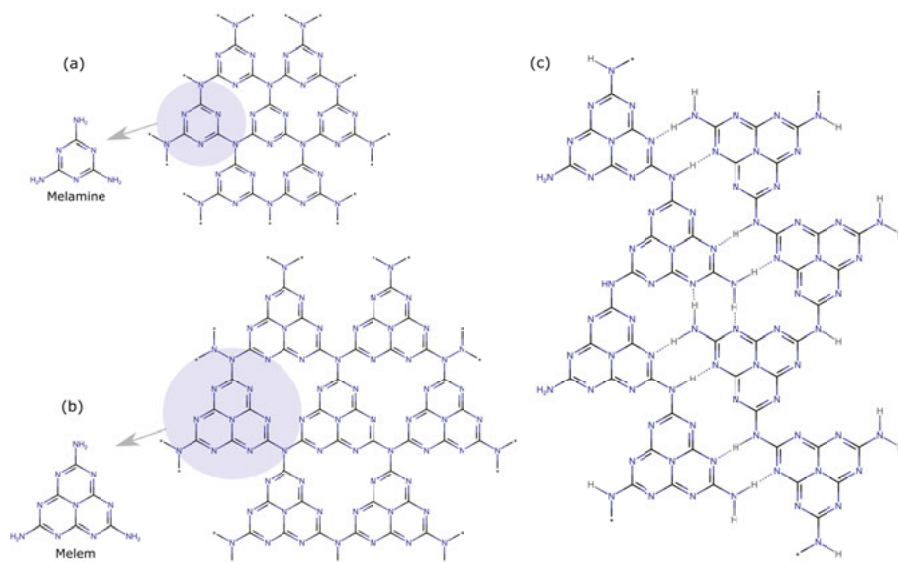
Figure 4.1. (a),(b) Binary Carbon Nitride (CN) based on melamine and melem units; c) 2D arrays of heptazine chains interacting via hydrogen-bonds. Adapted with permission from V. Lanzilotto, J. Luis Silva *et al.* [70] Copyright (2018) John Wiley and Sons.

interaction between periodic images. The JS approach has shown to provide accurate C 1s and N 1s XPS signatures [107, 108, 71].

From the experimental measurements, the differences between IE and BE indicates that the H-donor (amino-N) is much more affected than the H-acceptor (pyridin-like N). The N 1s core-level BE was simulated for H-bonded structures by increasing the number of melamine units. We considered monomer, dimer, trimer, and a stable hexagonal arrangement. Previous STM study observations indicate that the hexagonal packing can be employed to model the thick film, and 1.2 ML sample [109]. Figure 4.3 mainly shows the relative chemical shifts where energy scales were calibrated from monomer and shifted to align the spectra using the peak at lower BEs as reference. The theory and experiment show a good agreement (chemical shifts between the -N=C and NH_2 bonds of 1.67 eV from theory and 1.51 eV from the experiment). However, experimental features not included in the simulations such as differences of structural vibrations between the $-NH_2$ and $-N = C$ units [110] could be responsible for 0.16 eV deviation. Table 4.1 shows the experimental and theoretical BE and chemical shifts for different bonds. The experimental spectrum shows a reduction of 0.66 eV from the gaseous melamine to the thick film, which is an excellent approximation compared to the theoretical (from gaseous to hexagonal structure) chemical shift of 0.51 eV.
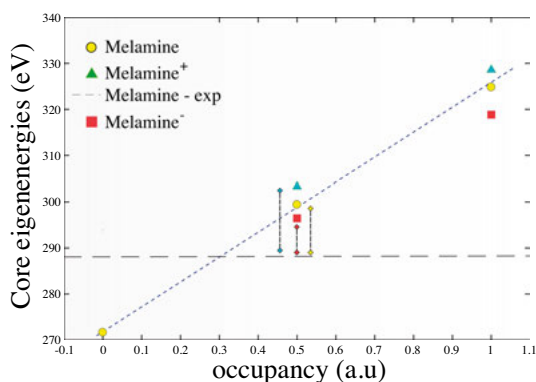
Figure 4.2. C 1s Core level shifts as a function of electron occupancy. The horizontal dashed line at ca 288 eV represents the experimental value for C 1s Melamine.

In Figure 4.3 (b), the N 1s signals from N-atoms inside the ring show small core-level shifts compared to signals from the monomer structure. However, N1s spectra from amino N-atoms involved in H-bonds (red color) shift by 0.7 eV to lower energies. Additionally, as predicted by Garcia-Gil *et al.* [111], the H-donors are more affected than H-acceptors since $-N = C$ components (green color) shifts by 0.1 eV to higher energies as compared to -N=C groups which are not directly interacting with H-atoms. Furthermore, the trimer shows an increasing number of N1s peaks derived from NHH components where small variations of length/angles (Figure 4.4 (a),(b), and (c)) could be responsible for the spread of signals. For the packed hexagonal structure at the bottom of Figure 4.3, we observe only two N1s components since only two functional groups are directly involved in hydrogen bonds. We have also observed small chemical shifts for N 1s between gas-phase and solid-state, regarding the nitrogen deriving from the amino group NH_2 and from the triazine

Table 4.1. *Experimental and Theoretical BE for C1s and N1s. The difference between experimental and theoretical values of N 1s compose the Core Level Shift between the -N=C and NH$_2$ bonds. Adapted with permission from V. Lanzilotto, J. Luis Silva et al. [70] Copyright (2018) John Wiley and Sons.*

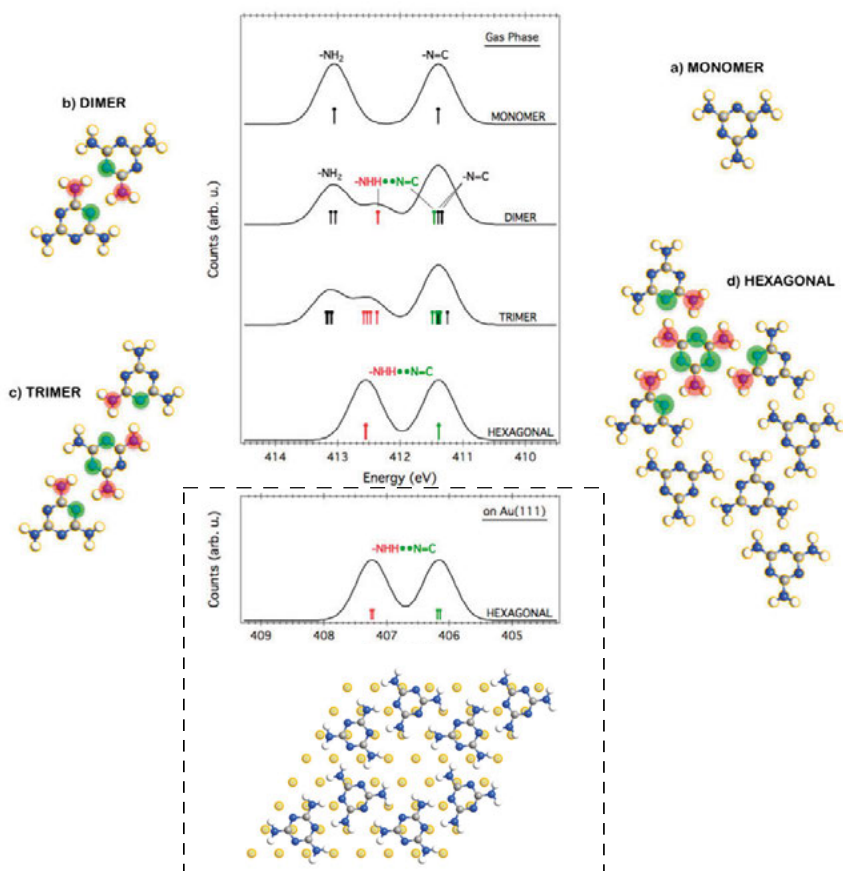| Binding Energy				
Line	**Bonding**	**Gas Phase**	**Thick Film**	**Monolayer**
C1s BE (eV)	-N=C	293.39	287.94	287.10
N1s BE (eV)	NH$_2$	405.50	399.38	398.75
N1s BE (eV)	-N=C	403.99	398.53	397.81
Core Level Shift				
Line	**Bonding**	**Gas Phase**	**Thick Film**	**Monolayer**
N 1s (EXP) (eV)	-	1.51	0.85	0.94
N 1s (TEO)(eV)	-	1.67	1.16	1.06

Figure 4.3. N1s XPS spectra for Melamine as a) Monomer, b) Dimer, c) Trimer, and d) stabilized hexagonal close-packed structure. Bottom: N1s for packed hexagonal structure on Au(111) surface. Adapted with permission from V. Lanzilotto, J. Luis Silva *et al.* [70] Copyright (2018) John Wiley and Sons.

$N = C$. The core-level shift decreases around 0.5 eV (from 1.5 to less than 1.0 eV).

Our calculations show a chemical shift of approximately 0.51 eV between gas-phase and thick film for the periodic hexagonal structure. Therefore, we have a deviation of 0.15 eV of the latter as compared to experimental chemical changes (0.66 eV) between thick film and gaseous Melamine, as shown in Table 4.1. We have also estimated the N1s spectrum for polymeric hexagonal-packed Melamine on top of the Au(111) surface, which only slightly decreases the chemical shift by 0.1 eV as compared to the surface without Au(111) substrate, as shown on Table 4.1. A comparison between theory and experiments shows a better agreement for the monolayer. The electronic structure of the H-donor(NH_2) is modified by hydrogen interacting through the amino group

H-bond	H••N (Å)	Angle (°)	BE –NH$_2$ (eV)	BE –C=N (eV)	Δ (eV)
N7-H••N9	1.96 Å	1.0°	412.07	411.17	0.90
N8-H••N2	1.96 Å	1.0°	412.07	411.17	0.90

H-bond	H••N (Å)	Angle (°)	BE –NH$_2$ (eV)	BE –C=N (eV)	Δ (eV)
N3-H••N8	2.06 Å	4.2°	411.35	410.19	1.16
N4-H••N2	2.06 Å	4.3°	411.35	410.19	1.16

H-bond	H••N (Å)	Angle (°)	BE –NH$_2$ (eV)	BE –C=N (eV)	Δ (eV)
(N10)-H••N5	2.20 Å	4.4°	412.53	411.30	1.23
(N18)-H••N15	2.20 Å	3.7°	412.47	411.36	1.11
(N7)-H••N3	2.04 Å	3.8°	412.41	411.31	1.10
(N2)-H••N17	1.96 Å	2.9°	412.32	411.42	0.90

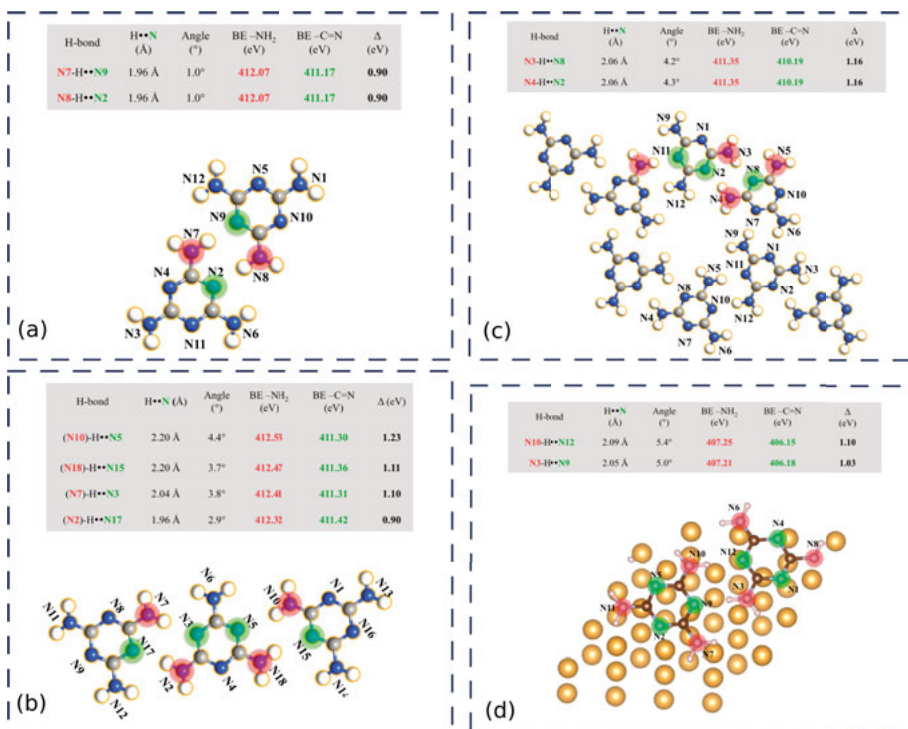| H-bond	H••N (Å)	Angle (°)	BE –NH$_2$ (eV)	BE –C=N (eV)	Δ (eV)
N10-H••N12	2.09 Å	5.4°	407.25	406.15	1.10
N3-H••N9	2.05 Å	5.0°	407.21	406.18	1.03

(a) (b) (c) (d)

Figure 4.4. H-bond, Angles, and N1s BE of specific N-atoms for Melamine (a) dimer, (b) trimer, (c) hexagonal, and (d) hexagonal packed on top of Au(111). Adapted with permission from V. Lanzilotto, J. Luis Silva *et al.* [70] Copyright (2018) John Wiley and Sons.

and the triazine N atom of the melamine molecule. Therefore the N 1s signal of the pyridine-like N-atoms remain very similar. We have studied the electronic structure of N-functional groups involved in H-bonds employing DFT calculations. For these cases, XPS signatures could capture the effects of g-C_3Ns_4 building blocks. Since it was possible to capture these spectroscopy trends, it will be interesting to extend these studies towards the investigations of spectroscopy properties of hybrid 2D structures with g-C_3N_4 as the catalyst over metallic supports by adding an explicit solvation model.

5. Spectroscopy properties of molecular electrocatalysts in aqueous environment

In this section, we investigate the XPS fingerprints of High-Valence Ruthenium-Oxo Complexes that exhibit complex proton-coupled electron transfer reactions such as those of the electro-catalytic water splitting processes (PAPER VI). In this work, we have characterized intermediates from $[RuII(bpy)_2(py)-(OH_2)]^{2+}$ electro-catalyst using XPS in the water environment along a specific reaction pathway with minimum intervention. It was necessary to develop a new methodology to analyze electrochemical properties and fingerprint possible signatures of these intermediates. The motivation is to investigate the spectroscopy properties of proton-coupled electron transfer reactions in an aqueous environment and identify fingerprints on the XPS spectroscopy of reaction intermediates using DFT. It is essential to highlight that we have followed the same procedure by using the Janak-Slater transition state approach to estimate the XPS.

5.1 Reaction Pathway for the model system $[RuII(bpy)_2(py)-(OH_2)]^{2+}$

The water-splitting reaction mechanism $2H_2O \rightarrow O_2 + 2H_2$ is carried with positive changes of the Gibbs free energy ($\Delta G = 2.46$ eV). The photon energy can be converted into chemical energy and stored through two possible half-step electrochemical mechanisms: (i) the oxygen evolution reaction (OER), where $2H_2O \rightarrow O_2 + 4H^+ + 4e^-$ and (ii) hydrogen evolution reaction (HER), where $4H^+ + 4e^- \rightarrow 2H_2$. This reaction is motivated by the photochemical energy conversion model from the natural Photosystem II (PSII), where the Mn_4CaO_5 catalyst clusters, embedded in a protein, performs the oxygen evolution, and the oxygen production rate stands in the interval of $100 - 400$ s^{-1}. The literature explores many approaches towards enhancing the water oxygen rate using Ru-based complexes, as well as the turnover number (TON) and turnover frequency (TOF) through the use of metal-based complexes [24, 25, 26]. The Ru-based complexes developed by Duan *et al.* showed an important improvement of TOF for intensities >1000 s$^-$1 [27, 28]. When considering the efficient
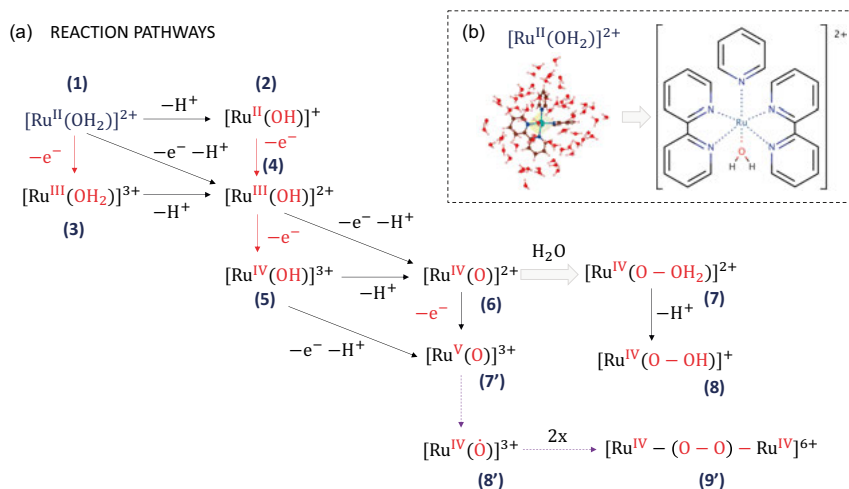
(a) REACTION PATHWAYS

(b) $[Ru^{II}(OH_2)]^{2+}$

$$[Ru^{II}(OH_2)]^{2+} \xrightarrow{-H^+} [Ru^{II}(OH)]^+$$

(1) **(2)**

$[Ru^{III}(OH_2)]^{3+}$ **(3)**

$[Ru^{III}(OH)]^{2+}$ **(4)**

$[Ru^{IV}(OH)]^{3+}$ **(5)**

$[Ru^{IV}(O)]^{2+}$ **(6)** $\xrightarrow{H_2O}$ $[Ru^{IV}(O-OH_2)]^{2+}$ **(7)**

$[Ru^{V}(O)]^{3+}$ **(7')**

$[Ru^{IV}(O-OH)]^+$ **(8)**

$[Ru^{IV}(\dot{O})]^{3+}$ **(8')** $\xrightarrow{2x}$ $[Ru^{IV}-(O-O)-Ru^{IV}]^{6+}$ **(9')**

Figure 5.1. (a) Possible reaction pathways of a model system [RuII(bpy)$_2$(py)-(OH$_2$)]$^{2+}$. (b) Snapshot from DFT calculations and schematic representation of the model [RuII(bpy)$_2$(py)-(OH$_2$)]$^{2+}$.

WOC design, the formation of species with O-O bond becomes extremely important as it modulates the efficiency of Photosystem II. The mechanism of formation can occur through either the water nucleophilic attack on metal-oxo units or association of two oxo units [30]. As previously discussed in the introduction, multiple oxidation reactions are necessary before reaching active high-valence states that drive water oxidation efficiently. Hence, the Ru-based complexes RuIV=O and RuV=O are critical intermediate steps towards forming the O-O bond. However, these intermediates are difficult to detect due to hyper-reactiveness. Duan *et al.* have explored possible activation pathway reactions of two metal-oxo coupled units [26], and recently, Pushkar *et al.* characterized the RuV=O through electron paramagnetic resonance [112]. Figure 5.1 (a) shows possible activation reaction pathways discussed in this work. We have investigated the target species [RuII(bpy)$_2$(py)-(OH$_2$)]$^{2+}$ (1), as well as the intermediates (2) [RuII(bpy)$_2$(py)-(OH)]$^+$ and (4) [RuIII(bpy)$_2$(py)-(OH)]$^{2+}$. Further, we have also investigated the species (6) [RuIV(bpy)$_2$(py)-(O)]$^{2+}$ after oxidation/deprotonation process derived from species (4). We have compared our results with results from X-ray spectroscopy experiments performed at synchrotron facilities under realistic conditions for probing these Ru-based model systems at high resolution. The comparison between theoretical and experimental results allowed us to investigate these molecular systems in the water environment. In the next section, we will investigate XPS properties in the water environment of the model system (1) and its corresponding intermediates (2), (4), and (6).

5.2 XPS fingerprints of Ru-based complexes along a reaction pathway in water environment
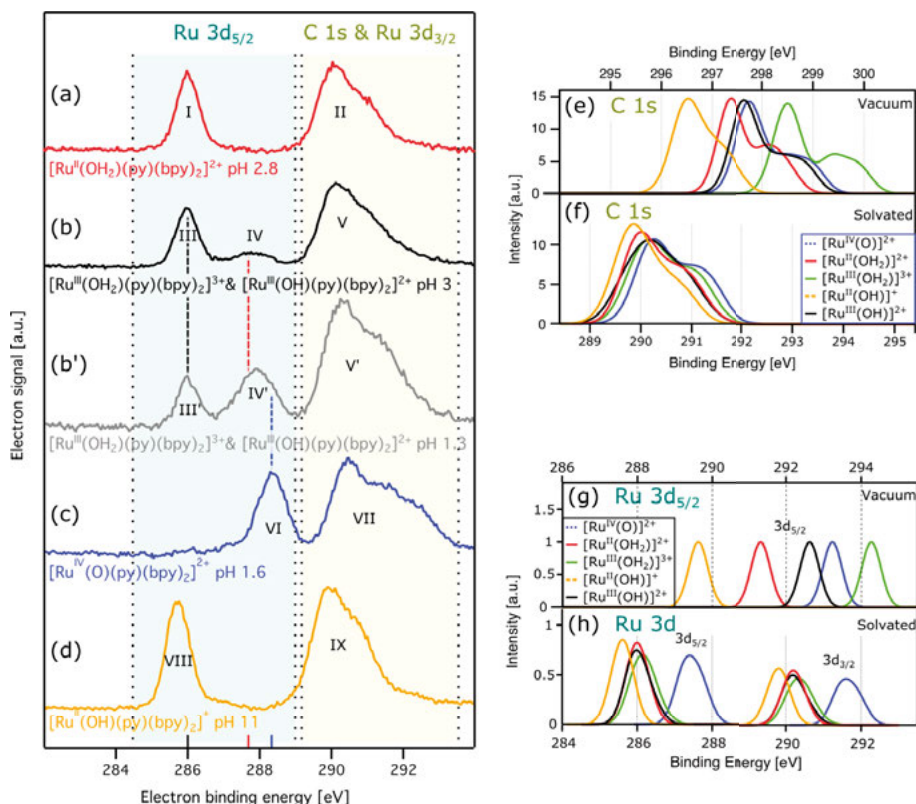

Figure 5.2. (a)-(d) Experimental XPS spectra of Ru 3d and C 1s using liquid-jets, (e) C 1s XPS spectra in the gas phase, (f) C 1s XPS spectra in aqueous solution, (g) Ru 3d 5/2 XPS spectra in the gas phase and (h) Ru 3d 5/2 XPS spectra using explicit solvation. Reprinted with permission from J. Luis Silva *et al.* [29] Copyright (2019) American Chemical Society.

Our model system $[RuII\text{-}OH_2]^{2+}$ was chemically oxidized to generate the species (2), (4), and (6) in solution, and added to the liquid jet. In contrast, the protonation of the species was controlled through the modulation of the pH. We have accessed the XPS spectra using a sequential approach combining first-principles optimization, Monte Carlo (MC) simulations using the DICE code [113], and x-ray photoelectron spectroscopy calculations. The experimental Figure 5.2 (a-d) shows the XPS spectra of the Ru 3d and C 1s and Figure 5.2 (e-h) shows the corresponding spectra calculated using our methodology. We have also resolved the XPS of Ru-based complexes under the influence of the aqueous environment (calculation details in reference [29]). For each simulation, we have used a cubic unit cell of 25, including

Table 5.1. *Experimental and theoretical values of the CLS in eV and its shifts as compared to the reference complex [RuII(OH2)(py)(bpy)$_2$]$^{2+}$. The theoretical values were shifted by -2.51eV. The parenthesis represents the labels of Figure 2 (a)-(d). The bracket includes the values of complexes with explicit water molecules. Adapted with permission from J. Luis Silva et al. [29] Copyright (2019) American Chemical Society.*

	Experimental		Theoretical			
			Vacuum		Solvated	
Ru 3d$_{5/2}$	BE	ΔBE	BE	ΔBE	BE	Δ BE
[RuII(OH)(py)(bpy)$_2$]$^+$	285.7 (VIII)	-0.3	289.6	-1.7	285.6	-0.4
[RuII(OH$_2$)(py)(bpy)$_2$]$^{2+}$	286.0 (I)	0.0	291.3 [290.9]	0.0[0.0]	286.0	0.0
[RuIII(OH)(py)(bpy)$_2$]$^{2+}$	286.0 (III)	0.0	292.6	1.3	286.0	0.0
[RuIII(OH$_2$)(py)(bpy)$_2$]$^{3+}$	287.7 (IV′)	1.7	294.2 [294.0]	2.9 [3.0]	286.3	0.3
[RuIV(O)(py)(bpy)$_2$]$^{2+}$	288.2 (VI)	2.2	293.2 [293.2]	1.9 [2.3]	287.5	1.5

the first solvation shell obtained from MC simulations. These uncorrelated clusters were selected from 100 configurations, and each snapshot contains 70 water molecules obtained with the Minimum Distance Distribution Function (MDDF) [114]. The Janak-Slater [73, 71] transition state approximation was employed (half-core occupation), as described before, to estimate the average of C 1s and Ru 3d spectra from 20 uncorrelated snapshots for each Ru complex. In our approach, we carried out 2600 [1] calculations to estimate averages of C 1s and Ru 3d. For each configuration, we have also estimated an average potential correction based on the vacuum levels by considering XYZ directions and performed the Bader analysis [76, 77, 115] to infer the electronic charge distributions. For each snapshot, the XPS signature is represented by a discrete set of core level transition states fitted with Gaussians using full width at half maximum (FWHM) of 0.6 eV. For each system, we have taken an average of the XPS signal considering 20 snapshots. These averages were calculated for different protonation and charged states of Ru-complexes to study the effects of the aqueous environment and critical physical-chemical properties.

Figure 5.2 (a), [RuII-OH$_2$]$^{2+}$ shows both peaks (I) and (II) which corresponds to the Ru 3d$_{\frac{5}{2}}$ orbital at 286 eV, and the partial overlapping of C 1s and Ru 3d$_{\frac{3}{2}}$ states around 290-291 eV, respectively. This signal was convoluted with a fixed experimental value for the spin-orbit coupling (SOC) of about 4.2 eV [116]. The Figures 5.2 (a) and (b) have very similar peaks of [RuII-OH$_2$]$^{2+}$ and [RuIII-OH]$^{2+}$, which can be explained by a charge compensation effect.

This compensation effect can be the result of two features: (i) by removing one electron from the system we can increase the net charge from the metallic center, and consequently, increase of the core level BE, and (ii) high donating profile of OH- that can lead to higher transfers of electron density to the metallic center and decrease of the BE. Therefore, the similarities between 5.2 (a)

---

[1]5 Ru based complexes * 25 C atoms * 20 snapshots, and the same for 1 Ru atom.
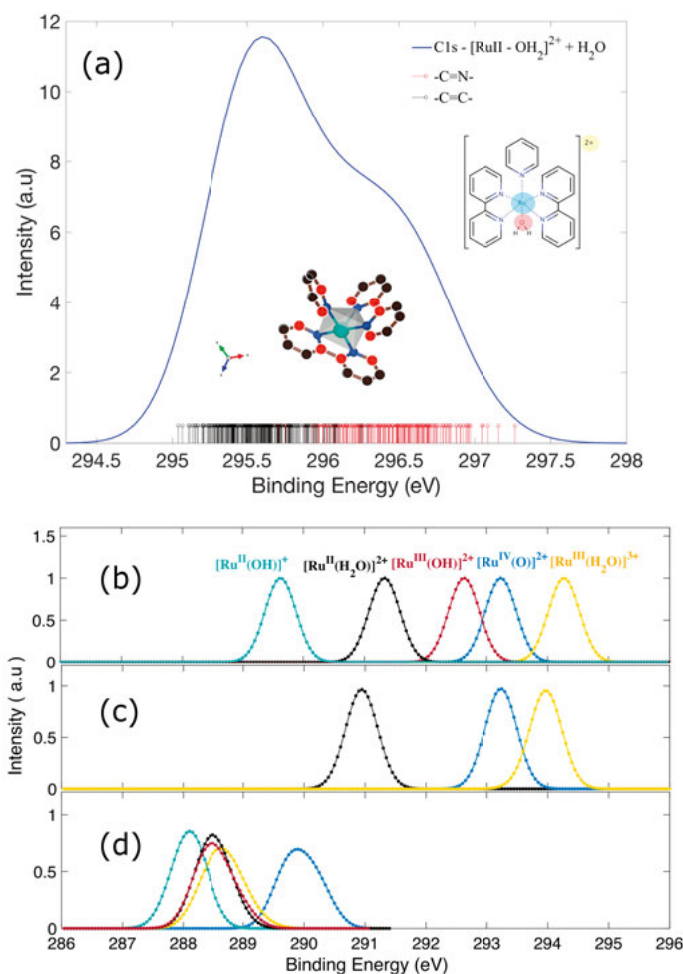
Figure 5.3. (a) Averaged C 1s spectra of the $[RuII=H_2O]^{2+}$ showing the contributions to specific bonds from different environments (20 snapshots). (b-d) Calculated Ru 3d5/2 XPS spectra in the gas phase, averaged from the ensemble of partial solvation and full solvation shell. Adapted with permission from J. Luis Silva *et al.* [29] Copyright (2019) American Chemical Society.

and (b) corresponds to compensation of both effects in the water environment. The large shift observed in Figure 5.2 (c) for $[RuIV=O]^{2+}$ species is the result of the solvation effects. Figure 5.2 (d) shows the XPS spectra of $[RuII-OH]^+$ species after deprotonation of $[RuII-OH_2]^{2+}$ under high pH values. The larger electron density of the metallic center that generates the Ru 3d5/2 peak (VIII)

as compared to the metallic center of $[\text{RuII-OH}_2]^{2+}$ indicates the shift of 0.3 eV toward lower BE as compared to peaks I and III.

Figure 5.2 (e) shows the calculated C 1s spectra in the gas phase of the reference model $[\text{RuII-OH}_2]^{2+}$ and its multiple oxidation states. The primary trend extracted from this Figure is associated with the net charge dependence of the peaks. The complexes with a 2+ charge display a reliance on the BEs based on the Ru oxidation states. However, the experimental findings do not post the same behavior. Figure 5.2 (f) shows that the inclusion of the solvation effect is critical to fingerprint these complexes in the water environment as it agrees with the experimental trend.

Figure 5.3 (a) shows the calculated average spectra composed by 20 snapshots of a specific fully solvated complex. The XPS spectra are generally shifted towards lower binding energies due to the solvation effect and dependent on the net charge. Additionally, the C 1s spectra are composed of two peaks separated by 1 eV due to two chemically non equivalent C atoms. These carbons are bonded to N with higher BE, and two other C atoms at lower BE, respectively. We separated the contributions of the C 1s BE for each type of bond, as shown in Figure 5.3 (a). Figure 5.3 (b-d) shows our calculated Ru 3d for the Ru complexes in the gas phase, partially solvated and fully solvated, respectively. We calculated the Ru 3d ensemble-averaged spectra using snapshots explicitly considering only the water molecules with hydrogens bonded to the hydroxo or the oxo ligand. The trend was analogous to that in the gas phase. We have obtained a similar pattern compared to the experimental results only when using a solvation shell of 70 water molecules. Therefore, the experimental results were explained only by the calculations carried out on the fully hydrated complexes. A comparison between the peaks can be assessed in Table 5.1. We have also used the snapshots from Monte Carlo simulations to statistically verify how the first-neighbors could affect the core-level binding energies. As previously explained in the theory section, the model is based on the multi-linear regression for the core-level shifts:

$$BE_{Ru} = \beta_2\, q_{Ru} + \beta_1 \sum_{i=0}^{K} \frac{q_i}{r_{i,Ru}} + \beta_0 \tag{5.1}$$

where the Bader Analysis is used to obtain the charges, q_{Ru} represents the Ru charge, q_i is the charge of first-neighbors, and r_i is the bond-length between the first neighbors (i) and the metallic center Ru. The parameters of the model were optimized to $\beta_0 = 285.51$ eV, $\beta_1 = 4.17$ eV and $\beta_2 = 1.06$ eV with high statistical significance of $R^2 = 0.82$.

Figure 5.4 displays the projection of the induced averaged potentials as a function of the Ru charge for each snapshot. The clustering indicates a trend for the charge of the metallic center Ru (increase in the x-axis) within the
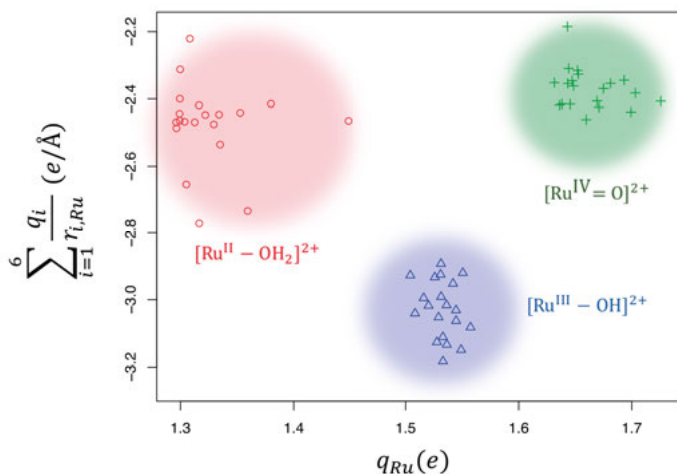
Figure 5.4. The plot of the potential induced by the first-neighbor atoms as a function of Ru charge. Reprinted with permission from J. Luis Silva *et al.* [29] Copyright (2019) American Chemical Society.

increment of the oxidation states (IV>III>II), such that $[RuIV=O]^{2+}$ >$[RuIII-OH]^{2+}$ > $[RuII-H_2O]^{2+}$. The model also provides consistent indications that the lower BEs of $[RuIII-OH]^{2+}$ are caused by a possible influence of the pyridine nitrogens. Therefore, the nitrogens would be capable of inducing shifts of the BEs toward lower absolute values. Further, the latter effect could also lead to the similarity observed between BEs of $[RuII-H_2O]^{2+}$ and $[RuIII-OH]^{2+}$. However, $[RuIV=O]^{2+}$ shows an average potential contribution that is closer to that of $[RuII-H_2O]^{2+}$ and provides the ground for higher BEs shifts of 3d signals for oxo complexes. The charge redistribution and averaged potential seems to be underestimated for $[RuIII-OH_2]^{3+}$ and $[RuIV=O]^{2+}$, as shown by the core-level shift discrepancies between the calculated and experimental results. However, comparing the charge redistribution as a function of ruthenium oxidation states with the changes in the explicit water effect, and dipolar interactions, enabled us to explain the energy differences between calculations in a vacuum and aqueous environment.

6. Conclusions

In this thesis, we have used DFT-based calculations to extract the properties of solid-liquid interfaces of both molecules and hybrid 2D material interfaces. At first, we have worked with signatures and trends that could help to model new electrocatalysts for HER. This joint theory-experiment effort allowed us further to explore and push some boundaries in the design of electrocatalysts. We have performed simulations of hybrid-type systems considering a charge injector/catalyst scheme in the first paper where we predicted that multiple factors such as intra and inter-layer electron transport, interface coupling, Schottky Barrier and differential free Gibbs energy (ΔG_{H^*}) for hydrogen adsorption could affect the overall HER performance [41]. In the second paper, using almost the same methodology, we have explored new materials based on Td-WTe_2/2H-MoS_2 with shallow Tafel slopes. In the third paper, we have explored hybrid systems beyond metals built from a bilayer of g-C_3N_4 coupled with of Td-WTe_2, 2H-MoS_2 and Graphene. We also estimated ΔG_H using an implicit solvation model to obtain more realistic signatures since real electrodes are in a water environment. Further, we analyzed the electronic structure, ΔG_H, SBHs, and interface induced dipoles by varying the number of hydrogen in the porous region. Our main results show that g-C_3N_4/Td-WTe_2 has filled states in the Fermi level is an indication of higher charge mobility. We have also found that ΔG_H between 2H-MoS_2/g-C_3N_4 and Td-WTe_2/g-C_3N_4 in the porous region are very similar. Therefore, the lower SBH found with both GGA and HSE06 for Td-WTe_2/g-C_3N_4, as compared to 2H-MoS_2/g-C_3N_4, indicates lower resistance for charge injection across the interface. Additionally, the induced dipoles along g-C_3N_4/Td-WTe_2 interfaces increases as a function of the number of hydrogen atoms in the catalyst. This favorable driving force for electron injection under higher hydrogen coverages might facilitate the catalytic activity. We conclude that Td-WTe_2/g-C_3N_4 could outperform an efficient electrocatalyst for hydrogen evolution reaction.

Additionally, we have also studied the XPS fingerprints and electronic structure of the gas phase melamine (monomer, dimer, trimer, and hexagonal packed arrangement), and the hexagonally packed melamine adsorbed on the Au(111) surface composed of a slab of 3 layers. By calculating the core-level binding energy shifts (Janak-Slater transition state approximation) and comparing with the experimental measurements, we were able to show that the H bonds affect in a different way the electronic structure of amino N and the pyridine like N,

which results in strong modifications as the ionization energy of the amino N 1s is reduced. These results are of primary importance to advance studies on melamine films in the water environment. In the last paper, we have accessed the C 1s and Ru 3d XPS signatures of high-valence Ruthenium-oxo complexes along a reaction pathway in the water environment using a combined theory-experiment approach. Herein, we have used a new theoretical methodology by combing DFT-based calculations and Monte Carlo Simulations (explicit water solution) to resolve the XPS in the aqueous environment and better understand the involved chemical shifts of the reference species $[Ru^{II}\text{-}OH_2]^{2+}$ and its respective PCET oxidation states. Among the initial results, the $[Ru^{II}\text{-}OH_2]^{2+}$ and $[Ru^{III}\text{-}OH]^{2+}$ species displayed very similar XPS signatures due to the interplay of the following effects: (i) increase of the Ru-center positive charge induced by oxidation processes, and (ii) the more substantial transfer of the electron density to Ru^{III} (higher donating character of hydroxo units).

Further, we have also found a substantial shift of the Ru 3d spectra of the $[Ru^{IV}\text{=}O]^{2+}$ species towards higher binding energies as compared to the other oxidation states along the reaction pathway. The chemical shift of $[Ru^{IV}\text{=}O]^{2+}$ is strongly affected by the polarization of water around the complexes (explicit solvation model) since its XPS signal displayed an excellent agreement with the experimental trends. This conclusion was possible due to the similarities between experimental trends and theoretical calculations considering the first solvation shell and the XPS ensemble average spectra. As a final step, we have also compared the outcome spectra using the nearest-neighbor potential contributions for the Ru 3d binding energies to explain the higher 3d-state shifts of the oxo complex. These results comprise new methodologies and a challenging backbone to simulate the design and efficiency of solid-liquid interface devices and molecular systems for OEC and HER catalysis.

7. Sammanfattning på svenska

I den här avhandlingen har vi arbetat med gränssnittet med fast vätska, adsorberade molekyler på ytan och solvatiserade komplex med DFT-beräkningar (Densitet Funktionsteori) för att hitta möjliga signaturer som kan hjälpa till att utforma lämpliga energimaterial. Mer specifikt har vi utforskat hybridelektrokatalysatorer från Td-WTe_2 och 2H-MoS_2 för väteutvecklingsreaktion (HER), där en gemensam teori-experimentmetod användes för att avslöja bidrag från enskilda faktorer till HER. Dessutom har vi avslöjat gränssnittseffekterna av hybridstrukturen Td-WTe_2/2H-MoS_2 och hybridelektrokatalysatorer baserade på g-C_3N_4. Användningen av kolbaserade strukturer och system bortom metaller för effektiv HER är fortfarande en utmaning, och g-C_3N_4 är en porös metallfri halvledare av polymer som kan användas för produktion av väte från vatten. Därför har vi studerat flera faktorer som kan påverka HER genom att använda effekten av vatten för hybridsystemen (katalysator / strömkollektor) g-C_3N_4/X, där X är Graphene, Td-WTe_2 och 2H-MoS_2. I dessa hybridkatalysatorer är den nuvarande samlaren sammansatt av en halvmetallisk struktur som ansvarar för att injicera laddningar i den primära katalysatorn g-C_3N_4, där förbrukningen av elektroner sker under väteutvecklingsreaktionen. Vidare har vi också studerat XPS-fingeravtryck av gasfas-melamin (monomer, dimer, trimer och hexagonalt packat arrangemang), hexagonalt packad melamin adsorberad på Au(111) -ytan och högvalens-ruteniumkomplex längs en reaktionsväg i vattenlösning genom en gemensam teori-experimentmetod.

I de två första artiklarna är fokuset på det gemensamma teori-experimentet för att distribuera nya hybridelektrokatalysatorer för väteutvecklingsreaktion (HER). I synnerhet behandlar det första uppsatsen ett enda skikt och system av hybridtyp som mikroreaktorer (strömkollektor/katalysatorer) för HER. Vi utforskar platsberoende beräkningar av en termodynamisk deskriptor för att uppskatta HER-aktiviteten, elektronisk struktur och Schottky Barrier Height (SBH) för att mäta motståndet för laddinjektion över gränssnittet. I det andra uppsatsen förutspådde vi ett nytt material som använder DFT-baserade trender, som är hybridelektrokatalysatorn Td-WTe_2/2H-MoS_2. I det tredje uppsatsen undersöker vi hybridsystem utöver metaller byggda från ett tvåskikt av g-C_3N_4 i kombination med Td-WTe_2, 2H-MoS_2 och Graphene. Vi har också uppskattat vätebindande fri energi ΔG_H med hjälp av en implicit solvationsmodell för att få mer realistiska signaturer. Vidare analyserade vi den elektroniska strukturen, ΔG_H, SBHs och gränssnittsinducerade dipoler genom

att variera antalet väte i den porösa regionen. Resultaten visar att g-C_3N_4/Td-WTe_2 har fyllt tillstånd på Fermi-nivån, vilket är en bra indikation på högre laddningsmobilitet. Vi har också funnit att ΔG_H mellan 2H-MoS_2/g-C_3N_4 och Td-WTe_2/g-C_3N_4 i den porösa regionen är liknande. SBH utvärderades med både GGA och HSE06-funktionerna för Td-WTe_2/g-C_3N_4 och jämfördes med 2H-MoS_2/g-C_3N_4. Våra beräkningar visar att Td-WTe_2/g-C_3N_4 har lägre motstånd för laddinjektion över gränssnittet. Dessutom ökar de inducerade dipolerna över g-C_3N_4/Td-WTe_2-gränssnitt som en funktion av antalet väteatomer i katalysatorn. Denna gynnsamma drivkraft för elektroninsprutning under högre vätetäckningar kan förbättra den katalytiska aktiviteten. Vi drar slutsatsen att Td-WTe_2/g-C_3N_4 kan klassificeras som en effektiv elektrokatalysator för väteutvecklingsreaktion.

I de två sista tidningarna undersöker vi XPS-fingeravtryck av molekylära och fast tillståndssystem genom de kemiska förändringarna av gasfasmelamin (monomer, dimer, trimer och hexagonal packad anordning) och den sexkantiga packningen av melamin adsorberad på Au (111) yta. Vi har använt DFT-baserade beräkningar för att uppskatta kärnnivåens bindningsenergiförskjutningar med hjälp av Janak Slater-övergångstillståndstillnärmningen, där vi har studerat den kemiska förändringen för varje kväveform. För triazinet N (melamin) bundet till H-givaren härledd från aminogruppen (NH_2) påverkas H-givarens elektroniska struktur starkt då joniseringsenergin för aminoen N 1 reduceras. I det sista uppsatsen har vi utvecklat en ny metodik genom att kombinera DFT-beräkningar med Monte Carlo-simuleringar med hjälp av uttrycklig solvation för att lösa XPS och förstå de kemiska förändringarna i [Ru ^{II}-OH_2]$^{2+}$ arter, såväl som av flera PCET-oxidationstillstånd. Bland de spännande resultaten har [Ru^{II}-OH_2]$^{2+}$ och [Ru^{III}-OH]$^{2+}$ arter visat liknande XPS-signaturer på grund av utbyte av två effekter: (i) ökning av den Ru-center positiva laddningen inducerad av oxidationsprocesser, och (ii) den mer betydande överföringen av elektrondensiteten till Ru^{III} (högre donationskaraktär hydroxidenheter). Vidare har Ru 3d-spektra för [Ru ^{IV}=O]$^{2+}$ arter visat betydande förändringar mot högre bindande energier jämfört med andra PCET-oxidationstillstånd längs den studerade reaktionsvägen. Detta arbete visar också att den kemiska förändringen av [Ru^{IV}=O]$^{2+}$ påverkas av polarisationen av den explicita solvationsmodellen, som bara kunde fånga den experimentella trenden med den kompletta första solvationen skal och ett XPS i genomsnitt medelvärde spektra över en viss mängd stillbilder från Monte Carlo-simuleringen. Till slutet visar vi också att de närmaste grannens potentiella bidrag till Ru 3d-bindande energier som uppstår från atomer runt metallcentret förklarar de högre 3D-tillståndsförskjutningarna i oxokomplexet.

8. Acknowledgments

First, I would like to thank my supervisors Moyses Araujo, Barbara Brena, and Olle Björneholm, for your patience, kind support, and opportunities during this challenging endeavor. It would be impossible to move forward with the projects and complete this thesis without your outstanding supervision and guidance during both comfortable and harder periods. I would also like to especially thank Moyses for the opportunity to do my Ph.D. in this incredible research environment, for bringing assertiveness, confidence, and expertise into our scientific discussions, and stimulate our group always to, no matter how to push the boundaries. Thank you for introducing and connecting me with researchers from across the world, and providing the resources necessary to present our projects at conferences in the USA, Sweden, Italy, and Brazil. I want to thank Susanne Mirbt for the honor of organizing the lunch seminars of our division. I really appreciate that, it was both an exciting and unique experience! Thank you for the full support during the last couple of months, sometimes we need that little push in the end, and you provided me with this when I most needed it.

Now, I would like to thank Ferreira for being a friend, a guru, for our talks, wise words, advice, and help. Thank you for the excitement regarding news about our personal life endeavors and projects, as well as to encourage us to pursue and be relentless as we move towards the scientific boundaries. I would also like to thank my friend Rodrigo, thank you for being there to whatever. The adaptation of moving abroad is hard, but we all have the histamine and perseverance to handle it. We fought many battles together during the bachelor's, and we have ended up in Sweden! Thank you for the friendship, I will always be around for whatever you need. Yocefu, thank you for the conversations and your friendship! From that little Lab (Laboratory of Optical Properties) in Brazil, I did not imagine that we would end up in Sweden. Rafael Barros, thank you for the friendship and for introducing me to VASP. I mean, everything started back there during that 10 min tutorial! So far, It is incredible how things evolved! Cleber, you are a unique multi-task human being. Thank you for providing our group with a semblance of "everything will be fine" and friendship. Olga, thank you for the talks, for visiting my family multiple times, engaging with my wife, and for bringing me wine during the "Russian girls party" while I was taking care of my newborn baby. I want to thank all my colleagues from the division, particularly John, Non,

Raghuveer, Bruno Ipaves, Ivan, Amitava, Giane, Emil, Mariia Pavliuk for the friendly discussions and Fika. I would also like to thank all our collaborators. I'm immensely grateful to share the co-authoring of these projects with your expertise.

I have a special thanks to my parents Sandra and Ze Lima, for the incredible support during my whole life. Thank you for the infinity talks, and for providing me with a model of dignity, ethics, hard work, perseverance, compassion, and many other qualities that I carry not only in my profession but also in my personal life. Despite our distance, we will always be together and aligned. My lovely grandmothers Licia and Railda, thank you for the prayers, to provide love, and to care for my family. During these 4+ years of my Ph.D., I have been far away from my son Vicente who lives in Brazil. Vicente, thank you for being psychologically strong and extremely patient with your father. You are always in my toughs, and I love you! During this time in Sweden, I have met my wife, Tatiana. We have got married, and we have had two kids, Alexander and Elisabeth. Tatiana, thank you for your love, care, and respect, I love you, Thank you for everything! My babies are too small to make sense of what is happening here, but I want to register that you are fantastic and bring light into our lives every day.

References

[1] John A Turner. Sustainable hydrogen production. *Science*, 305(5686):972–974, 2004.

[2] Seth Dunn. Hydrogen futures: toward a sustainable energy system. *International Journal of Hydrogen Energy*, 27(3):235–264, 2002.

[3] Dehui Deng, KS Novoselov, Qiang Fu, Nanfeng Zheng, Zhongqun Tian, and Xinhe Bao. Catalysis with two-dimensional materials and their heterostructures. *Nature Nanotechnology*, 11(3):218–230, 2016.

[4] Daniel G Nocera. The artificial leaf. *Accounts of Chemical Research*, 45(5):767–776, 2012.

[5] James Barber. Photosynthetic energy conversion: natural and artificial. *Chemical Society Reviews*, 38(1):185–196, 2009.

[6] Sophie Romain, Laura Vigara, and Antoni Llobet. Oxygen- oxygen bond formation pathways promoted by ruthenium complexes. *Accounts of Chemical Research*, 42(12):1944–1953, 2009.

[7] Yasufumi Umena, Keisuke Kawakami, Jian-Ren Shen, and Nobuo Kamiya. Crystal structure of oxygen-evolving photosystem II at a resolution of 1.9. *Nature*, 473(7345):55–60, 2011.

[8] G Charles Dismukes, Robin Brimblecombe, Greg AN Felton, Ruslan S Pryadun, John E Sheats, Leone Spiccia, and Gerhard F Swiegers. Development of bioinspired Mn_4O_4- cubane water oxidation catalysts: lessons from photosynthesis. *Accounts of Chemical Research*, 42(12):1935–1943, 2009.

[9] Markus D Karkas, Oscar Verho, Eric V Johnston, and Björn Åkermark. Artificial photosynthesis: molecular systems for catalytic water oxidation. *Chemical Reviews*, 114(24):11863–12001, 2014.

[10] Biaobiao Zhang and Licheng Sun. Why nature chose the Mn_4CaO_5 cluster as water-splitting catalyst in photosystem II: a new hypothesis for the mechanism of O–O bond formation. *Dalton Transactions*, 47(41):14381–14387, 2018.

[11] Thomas Kuntzleman and Charles F Yocum. Reduction-induced inhibition and Mn (II) release from the photosystem II oxygen-evolving complex by hydroquinone or NH_2OH are consistent with a Mn (III)/Mn (III)/Mn (IV)/Mn (IV) oxidation state for the dark-adapted enzyme. *Biochemistry*, 44(6):2129–2142, 2005.

[12] SW Gersten, GJ Samuels, and TJ Meyer. Highly efficient and robust molecular water oxidation catalysts based on ruthenium complexes. *J. Am. Chem. Soc*, 104:4029–4030, 1982.

[13] Rosalie K Hocking, Robin Brimblecombe, Lan-Yun Chang, Archana Singh, Mun Hon Cheah, Chris Glover, William H Casey, and Leone Spiccia. Water-oxidation catalysis by manganese in a geochemical-like cycle. *Nature Chemistry*, 3(6):461–466, 2011.

[14] Feng Jiao and Heinz Frei. Nanostructured cobalt oxide clusters in mesoporous silica as efficient oxygen-evolving catalysts. *Angewandte Chemie*, 121(10):1873–1876, 2009.

[15] Denys Shevchenko, Magnus F Anderlund, Anders Thapper, and Stenbjörn Styring. Photochemical water oxidation with visible light using a cobalt containing catalyst. *Energy & Environmental Science*, 4(4):1284–1287, 2011.

[16] Derek J Wasylenko, Chelladurai Ganesamoorthy, Javier Borau-Garcia, and Curtis P Berlinguette. Electrochemical evidence for catalyticwater oxidation mediated by a high-valent cobalt complex. *Chemical Communications*, 47(14):4249–4251, 2011.

[17] Dilek K Dogutan, Robert McGuire Jr, and Daniel G Nocera. Electocatalytic water oxidation by cobalt (III) hangman β-octafluoro corroles. *Journal of the American Chemical Society*, 133(24):9178–9180, 2011.

[18] Qiushi Yin, Jeffrey Miles Tan, Claire Besson, Yurii V Geletii, Djamaladdin G Musaev, Aleksey E Kuznetsov, Zhen Luo, Ken I Hardcastle, and Craig L Hill. A fast soluble carbon-free molecular water oxidation catalyst based on abundant metals. *Science*, 328(5976):342–345, 2010.

[19] Neal D McDaniel, Frederick J Coughlin, Leonard L Tinker, and Stefan Bernhard. Cyclometalated iridium (III) aquo complexes: efficient and tunable catalysts for the homogeneous oxidation of water. *Journal of the American Chemical Society*, 130(1):210–217, 2008.

[20] Jonathan F Hull, David Balcells, James D Blakemore, Christopher D Incarvito, Odile Eisenstein, Gary W Brudvig, and Robert H Crabtree. Highly active and robust Cp* iridium complexes for catalytic water oxidation. *Journal of the American Chemical Society*, 131(25):8730–8731, 2009.

[21] Ralte Lalrempuia, Neal D McDaniel, Helge Müller-Bunz, Stefan Bernhard, and Martin Albrecht. Water oxidation catalyzed by strong carbene-type donor-ligand complexes of iridium. *Angewandte Chemie International Edition*, 49(50):9765–9768, 2010.

[22] Julio Lloret Fillol, Zoel Codolà, Isaac Garcia-Bosch, Laura Gómez, Juan José Pla, and Miquel Costas. Efficient water oxidation catalysts based on readily available iron coordination complexes. *Nature Chemistry*, 3(10):807–813, 2011.

[23] W Chadwick Ellis, Neal D McDaniel, Stefan Bernhard, and Terrence J Collins. Fast water oxidation using iron. *Journal of the American Chemical Society*, 132(32):10990–10991, 2010.

[24] Javier J Concepcion, Jonah W Jurss, M Kyle Brennaman, Paul G Hoertz, Antonio Otávio T Patrocinio, Neyde Yukie Murakami Iha, Joseph L Templeton, and Thomas J Meyer. Making oxygen with ruthenium complexes. *Accounts of Chemical Research*, 42(12):1954–1965, 2009.

[25] James D Blakemore, Robert H Crabtree, and Gary W Brudvig. Molecular catalysts for water oxidation. *Chemical Reviews*, 115(23):12974–13005, 2015.

[26] Lele Duan, Carlos Moyses Araujo, Mårten SG Ahlquist, and Licheng Sun. Highly efficient and robust molecular ruthenium catalysts for water oxidation. *Proceedings of the National Academy of Sciences*, 109(39):15584–15588, 2012.

[27] Lele Duan, Fernando Bozoglian, Sukanta Mandal, Beverly Stewart, Timofei

Privalov, Antoni Llobet, and Licheng Sun. A molecular ruthenium catalyst with water-oxidation activity comparable to that of photosystem II. *Nature Chemistry*, 4(5):418–423, 2012.

[28] Lei Wang, Lele Duan, Ying Wang, Mårten SG Ahlquist, and Licheng Sun. Highly efficient and robust molecular water oxidation catalysts based on ruthenium complexes. *Chemical Communications*, 50(85):12947–12950, 2014.

[29] J. Luis Silva, Isaak Unger, Tiago Araujo Matias, Leandro Rezende Franco, Giane Damas, Luciano T Costa, Kalil CF Toledo, Tulio CR Rocha, Arnaldo Naves de Brito, Clara-Magdalena Saak, Kaline Coutinho, Koiti Araki, Olle Bjorneholm, Barbara Brena, and C. Moyses Araujo. X-ray Photoelectron Fingerprints of High-Valence Ruthenium–Oxo Complexes along the Oxidation Reaction Pathway in an Aqueous Environment. *The Journal of Physical Chemistry Letters*, 10(24):7636–7643, 2019.

[30] David W Shaffer, Yan Xie, and Javier J Concepcion. O–O bond formation in ruthenium-catalyzed water oxidation: single-site nucleophilic attack vs. O–O radical coupling. *Chemical Society Reviews*, 46(20):6170–6193, 2017.

[31] Emiliana Fabbri, Daniel F Abbott, Maarten Nachtegaal, and Thomas J Schmidt. Operando X-ray absorption spectroscopy: A powerful tool toward water splitting catalyst development. *Current Opinion in Electrochemistry*, 5(1):20–26, 2017.

[32] D Frank Ogletree, Hendrik Bluhm, Eleonore D Hebenstreit, and Miquel Salmeron. Photoelectron spectroscopy under ambient pressure and temperature conditions. *Nuclear Instruments and Methods in Physics Research Section A: Accelerators, Spectrometers, Detectors and Associated Equipment*, 601(1-2):151–160, 2009.

[33] Robert Seidel, Marvin N Pohl, Hebatallah Ali, Bernd Winter, and Emad F Aziz. Advances in liquid phase soft-x-ray photoemission spectroscopy: A new experimental setup at BESSY II. *Review of Scientific Instruments*, 88(7):073107, 2017.

[34] Robert Seidel, Stephan Thurmer, and Bernd Winter. Photoelectron spectroscopy meets aqueous solution: studies from a vacuum liquid microjet. *The Journal of Physical Chemistry Letters*, 2(6):633–641, 2011.

[35] Kaline Coutinho, Sylvio Canuto, and MC Zerner. A Monte Carlo-quantum mechanics study of the solvatochromic shifts of the lowest transition of benzene. *The Journal of Chemical Physics*, 112(22):9874–9880, 2000.

[36] Sylvio Canuto. *Solvation effects on molecules and biomolecules: computational methods and applications*, volume 6. Springer Science & Business Media, 2010.

[37] Jeff Greeley, Thomas F Jaramillo, Jacob Bonde, IB Chorkendorff, and Jens K Nørskov. Computational high-throughput screening of electrocatalytic materials for hydrogen evolution. *Nature materials*, 5(11):909–913, 2006.

[38] Zhi Wei Seh, Jakob Kibsgaard, Colin F Dickens, IB Chorkendorff, Jens K Nørskov, and Thomas F Jaramillo. Combining theory and experiment in electrocatalysis: Insights into materials design. *Science*, 355(6321), 2017.

[39] Charlie Tsai, Frank Abild-Pedersen, and Jens K Nørskov. Tuning the MoS_2 edge-site activity for hydrogen evolution via support interactions. *Nano letters*,

14(3):1381–1387, 2014.

[40] Charlie Tsai, Karen Chan, Frank Abild-Pedersen, and Jens K Nørskov. Active edge sites in MoSe$_2$ and WSe$_2$ catalysts for the hydrogen evolution reaction: a density functional study. *Physical Chemistry Chemical Physics*, 16(26):13156–13164, 2014.

[41] Yu Zhou, J. Luis Silva, John M Woods, Joshua V Pondick, Qingliang Feng, Zhixiu Liang, Wen Liu, Li Lin, Bingchen Deng, Barbara Brena, et al. Revealing the contribution of individual factors to hydrogen evolution reaction catalytic activity. *Advanced Materials*, 30(18):1706076, 2018.

[42] Xinchen Wang, Kazuhiko Maeda, Arne Thomas, Kazuhiro Takanabe, Gang Xin, Johan M Carlsson, Kazunari Domen, and Markus Antonietti. A metal-free polymeric photocatalyst for hydrogen production from water under visible light. *Nature materials*, 8(1):76–80, 2009.

[43] Mingshan Fan, Chengjie Song, Tianjun Chen, Xu Yan, Dongbo Xu, Wei Gu, Weidong Shi, and Lisong Xiao. Visible-light-drived high photocatalytic activities of Cu/g-C$_3$N$_4$ photocatalysts for hydrogen production. *RSC advances*, 6(41):34633–34640, 2016.

[44] Wee-Jun Ong, Lling-Lling Tan, Yun Hau Ng, Siek-Ting Yong, and Siang-Piao Chai. Graphitic carbon nitride (g-C$_3$N$_4$)-based photocatalysts for artificial photosynthesis and environmental remediation: are we a step closer to achieving sustainability? *Chemical Reviews*, 116(12):7159–7329, 2016.

[45] J. Luis Silva, Barbara Brena, and C. Moyses Araujo. g-C$_3$N$_4$/WTe$_2$ Hybrid Electrocatalyst for Efficient Hydrogen Evolution Reaction. *The Journal of Physical Chemistry C*, 124(16):8726–8735, 2020.

[46] Max Born and Robert Oppenheimer. Zur quantentheorie der molekeln. *Annalen der Physik*, 389(20):457–484, 1927.

[47] Pierre Hohenberg and Walter Kohn. Inhomogeneous electron gas. *Physical Review*, 136(3B):B864, 1964.

[48] Mel Levy. Universal variational functionals of electron densities, first-order density matrices, and natural spin-orbitals and solution of the v-representability problem. *Proceedings of the National Academy of Sciences*, 76(12):6062–6065, 1979.

[49] Walter Kohn and Lu Jeu Sham. Self-consistent equations including exchange and correlation effects. *Physical Review*, 140(4A):A1133, 1965.

[50] Michael Springboarg. *Methods of Electronic Structure Calculations*. John Wiley, 1th edition, 2000.

[51] David M Ceperley and Berni J Alder. Ground state of the electron gas by a stochastic method. *Physical Review Letters*, 45(7):566, 1980.

[52] John P Perdew and Alex Zunger. Self-interaction correction to density-functional approximations for many-electron systems. *Physical Review B*, 23(10):5048, 1981.

[53] Li Rao, Hongwei Ke, Gang Fu, Xin Xu, and Yijing Yan. Performance of several density functional theory methods on describing hydrogen-bond interactions. *Journal of Chemical Theory and Computation*, 5(1):86–96, 2009.

[54] Ulf von Barth and Lars Hedin. A local exchange-correlation potential for the spin polarized case. i. *Journal of Physics C: Solid State Physics*, 5(13):1629, 1972.

[55] Seymour H Vosko, Leslie Wilk, and Marwan Nusair. Accurate spin-dependent electron liquid correlation energies for local spin density calculations: a critical analysis. *Canadian Journal of Physics*, 58(8):1200–1211, 1980.

[56] John P Perdew, Kieron Burke, and Matthias Ernzerhof. Generalized gradient approximation made simple. *Physical Review Letters*, 77(18):3865, 1996.

[57] John P Perdew, John A Chevary, Sy H Vosko, Koblar A Jackson, Mark R Pederson, Dig J Singh, and Carlos Fiolhais. Atoms, molecules, solids, and surfaces: Applications of the generalized gradient approximation for exchange and correlation. *Physical Review B*, 46(11):6671, 1992.

[58] Bjørk Hammer, Karsten Wedel Jacobsen, and Jens Kehlet Nørskov. Role of nonlocal exchange correlation in activated adsorption. *Physical Review Letters*, 70(25):3971, 1993.

[59] Aliaksandr V Krukau, Oleg A Vydrov, Artur F Izmaylov, and Gustavo E Scuseria. Influence of the exchange screening parameter on the performance of screened hybrid functionals. *The Journal of Chemical Physics*, 125(22):224106, 2006.

[60] Georg Kresse and Daniel Joubert. From ultrasoft pseudopotentials to the projector augmented-wave method. *Physical Review B*, 59(3):1758, 1999.

[61] Peter E Blöchl. Projector augmented-wave method. *Physical Review B*, 50(24):17953, 1994.

[62] Sándor Kristyán and Péter Pulay. Can (semi) local density functional theory account for the London dispersion forces? *Chemical Physics Letters*, 229(3):175–180, 1994.

[63] Stefan Grimme. Accurate description of van der Waals complexes by density functional theory including empirical corrections. *Journal of Computational Chemistry*, 25(12):1463–1473, 2004.

[64] Alexandre Tkatchenko and Matthias Scheffler. Accurate molecular van der Waals interactions from ground-state electron density and free-atom reference data. *Physical Review Letters*, 102(7):073005, 2009.

[65] Stefan Grimme, Jens Antony, Stephan Ehrlich, and Helge Krieg. A consistent and accurate ab initio parametrization of density functional dispersion correction (DFT-D) for the 94 elements H-Pu. *The Journal of Chemical Physics*, 132(15):154104, 2010.

[66] Stefan Grimme. Semiempirical GGA-type density functional constructed with a long-range dispersion correction. *Journal of Computational Chemistry*, 27(15):1787–1799, 2006.

[67] Carsten Rostgaard. The projector augmented-wave method. *arXiv preprint arXiv:0910.1921*, 2009.

[68] K. Mathew, V. S. Chaitanya Kolluru, and R. G. Hennig. Vaspsol: Implicit solvation and electrolyte model for density-functional theory. `https://github.com/henniggroup/VASPsol`, 2018.

[69] K. Mathew, R. Sundararaman, K. Letchworth-Weaver, T. A. Arias, and R. G. Hennig. Implicit solvation model for density-functional study of nanocrystal surfaces and reaction pathways. *J. Chem. Phys.*, 140:084106, 2014.

[70] Valeria Lanzilotto, J. Luis Silva, Teng Zhang, Matuš Stredansky, Cesare Grazioli, Konstantin Simonov, Erika Giangrisostomi, Ruslan Ovsyannikov, Monica De Simone, Marcello Coreno, C. Moyses Araujo, Barbara Brena, and

Carla Puglia. Spectroscopic Fingerprints of Intermolecular H-Bonding Interactions in Carbon Nitride Model Compounds. *Chemistry–A European Journal*, 24(53):14198–14206, 2018.

[71] Noèlia Pueyo Bellafont, Francesc Viñes, Wolfgang Hieringer, and Francesc Illas. Predicting core level binding energies shifts: Suitability of the projector augmented wave approach as implemented in VASP. *Journal of Computational Chemistry*, 38(8):518–522, 2017.

[72] Lukas Köhler and Georg Kresse. Density functional study of CO on Rh (111). *Physical Review B*, 70(16):165405, 2004.

[73] JF Janak. Proof that $\delta e/\delta n = \varepsilon$ in density-functional theory. *Physical Review B*, 18:7165–7168, 1978.

[74] Weine Olovsson, Christian Göransson, Tobias Marten, and Igor A Abrikosov. Core-level shifts in complex metallic systems from first principle. *Physica Status Solidi (B)*, 243(11):2447–2464, 2006.

[75] Mike C Payne, Michael P Teter, Douglas C Allan, TA Arias, and ad JD Joannopoulos. Iterative minimization techniques for ab initio total-energy calculations: molecular dynamics and conjugate gradients. *Reviews of Modern Physics*, 64(4):1045, 1992.

[76] Richard FW Bader. Atoms in molecules. *Accounts of Chemical Research*, 18(1):9–15, 1985.

[77] Graeme Henkelman, Andri Arnaldsson, and Hannes Jónsson. A fast and robust algorithm for Bader decomposition of charge density. *Computational Materials Science*, 36(3):354–360, 2006.

[78] Andrew J Medford, Aleksandra Vojvodic, Jens S Hummelshøj, Johannes Voss, Frank Abild-Pedersen, Felix Studt, Thomas Bligaard, Anders Nilsson, and Jens K Nørskov. From the Sabatier principle to a predictive theory of transition-metal heterogeneous catalysis. *Journal of Catalysis*, 328:36–42, 2015.

[79] Kiran Mathew, Ravishankar Sundararaman, Kendra Letchworth-Weaver, TA Arias, and Richard G Hennig. Implicit solvation model for density-functional study of nanocrystal surfaces and reaction pathways. *The Journal of Chemical Physics*, 140(8):084106, 2014.

[80] Peter Atkins, Julio De Paula, and James Keeler. *Atkins' physical chemistry*. Oxford university press, 2018.

[81] Bjørk Hammer and Jens K Norskov. Why gold is the noblest of all the metals. *Nature*, 376(6537):238–240, 1995.

[82] Bjørk Hammer and Jens Kehlet Nørskov. Theoretical surface science and catalysis - calculations and concepts. In *Advances in Catalysis*, volume 45, pages 71–129. Elsevier, 2000.

[83] Lars Gunnar Moody Pettersson and Anders Nilsson. A molecular perspective on the d-band model: synergy between experiment and theory. *Topics in Catalysis*, 57(1-4):2–13, 2014.

[84] Raymond T Tung. The physics and chemistry of the schottky barrier height. *Applied Physics Reviews*, 1(1):011304, 2014.

[85] Xiaoyan Guo, Guohui Yang, Junfeng Zhang, and Xiaohong Xu. Structural, mechanical and electronic properties of in-plane 1T/2H phase interface of MoS_2 heterostructures. *AIP Advances*, 5(9):097174, 2015.

[86] Thomas F Jaramillo, Kristina P Jørgensen, Jacob Bonde, Jane H Nielsen, Sebastian Horch, and Ib Chorkendorff. Identification of active edge sites for electrochemical H_2 evolution from MoS_2 nanocatalysts. *Science*, 317(5834):100–102, 2007.

[87] Haotian Wang, Charlie Tsai, Desheng Kong, Karen Chan, Frank Abild-Pedersen, Jens K Nørskov, and Yi Cui. Transition-metal doped edge sites in vertically aligned MoS_2 catalysts for enhanced hydrogen evolution. *Nano Research*, 8(2):566–575, 2015.

[88] Chia-Hui Lee, Eduardo Cruz Silva, Lazaro Calderin, Minh An T Nguyen, Matthew J Hollander, Brian Bersch, Thomas E Mallouk, and Joshua A Robinson. Tungsten Ditelluride: a layered semimetal. *Scientific Reports*, 5:10013, 2015.

[89] Jens Kehlet Nørskov, Thomas Bligaard, Ashildur Logadottir, JR Kitchin, Jingguang G Chen, S Pandelov, and U Stimming. Trends in the exchange current for hydrogen evolution. *Journal of The Electrochemical Society*, 152(3):J23, 2005.

[90] Hongxia Zhong, Ruge Quhe, Yangyang Wang, Zeyuan Ni, Meng Ye, Zhigang Song, Yuanyuan Pan, Jinbo Yang, Li Yang, Ming Lei, et al. Interfacial properties of monolayer and bilayer MoS_2 contacts with metals: beyond the energy band calculations. *Scientific Reports*, 6:21786, 2016.

[91] Cheng Gong, Luigi Colombo, Robert M Wallace, and Kyeongjae Cho. The unusual mechanism of partial fermi level pinning at metal–MoS_2 interfaces. *Nano Letters*, 14(4):1714–1720, 2014.

[92] Yu Zhou, Joshua V Pondick, J. Luis Silva, John M Woods, David J Hynek, Grace Matthews, Xin Shen, Qingliang Feng, Wen Liu, Zhixing Lu, et al. Unveiling the interfacial effects for enhanced hydrogen evolution reaction on MoS_2/WTe_2 hybrid structures. *Small*, 15(19):1900078, 2019.

[93] J Gracia and P Kroll. Corrugated layered heptazine-based carbon nitride: the lowest energy modifications of c_3n_4 ground state. *Journal of Materials Chemistry*, 19(19):3013–3019, 2009.

[94] TS Miller, A Belen Jorge, TM Suter, A Sella, F Cora, and PF McMillan. Carbon nitrides: synthesis and characterization of a new class of functional materials. *Physical Chemistry Chemical Physics*, 19(24):15613–15638, 2017.

[95] Anke Schwarzer, Tatyana Saplinova, and Edwin Kroke. Tri-s-trizines (s-heptazines)-from a mystery molecule to industrially relevant carbon nitride materials. *Coordination Chemistry Reviews*, 257(13-14):2032–2062, 2013.

[96] Guoping Gao, Yan Jiao, Fengxian Ma, Yalong Jiao, Eric Waclawik, and Aijun Du. Metal-free graphitic carbon nitride as mechano-catalyst for hydrogen evolution reaction. *Journal of Catalysis*, 332:149–155, 2015.

[97] Wei Fu, Haiyong He, Zhuhua Zhang, Chunyang Wu, Xuewen Wang, Hong Wang, Qingsheng Zeng, Linfeng Sun, Xingli Wang, Jiadong Zhou, et al. Strong interfacial coupling of $MoS_2/g-C_3N_4$ van de Waals solids for highly active water reduction. *Nano Energy*, 27:44–50, 2016.

[98] Xinru Li, Ying Dai, Yandong Ma, Shenghao Han, and Baibiao Huang. Graphene/$g-C_3N_4$ bilayer: considerable band gap opening and effective band structure engineering. *Physical Chemistry Chemical Physics*, 16(9):4230–4235, 2014.

[99] Isis Ledezma-Yanez and Marc TM Koper. Influence of water on the hydrogen evolution reaction on a gold electrode in acetonitrile solution. *Journal of Electroanalytical Chemistry*, 793:18–24, 2017.

[100] Nicolas Dubouis and Alexis Grimaud. The hydrogen evolution reaction: from material to interfacial descriptors. *Chemical Science*, 10(40):9165–9181, 2019.

[101] Wenchao Sheng, Hubert A Gasteiger, and Yang Shao-Horn. Hydrogen oxidation and evolution reaction kinetics on platinum: acid vs alkaline electrolytes. *Journal of The Electrochemical Society*, 157(11):B1529, 2010.

[102] Yang Jiao, Anders Hellman, Yurui Fang, Shiwu Gao, and Mikael Käll. Schottky barrier formation and band bending revealed by first-principles calculations. *Scientific Reports*, 5:11374, 2015.

[103] Xinchen Wang, Kazuhiko Maeda, Arne Thomas, Kazuhiro Takanabe, Gang Xin, Johan M Carlsson, Kazunari Domen, and Markus Antonietti. A metal-free polymeric photocatalyst for hydrogen production from water under visible light. *Nature Materials*, 8(1):76–80, 2009.

[104] Vijay S Vyas, Vincent Wing-hei Lau, and Bettina V Lotsch. Soft photocatalysis: organic polymers for solar fuel production. *Chemistry of Materials*, 28(15):5191–5204, 2016.

[105] AP Dementjev, A De Graaf, MCM Van de Sanden, KI Maslakov, AV Naumkin, and AA Serov. X-ray photoelectron spectroscopy reference data for identification of the C_3N_4 phase in carbon–nitrogen films. *Diamond and related materials*, 9(11):1904–1907, 2000.

[106] M Mura, N Martsinovich, and L Kantorovich. Theoretical study of melamine superstructures and their interaction with the Au (111) surface. *Nanotechnology*, 19(46):465704, 2008.

[107] Roberto Carlos Salvarezza and Pilar Carro. Exploring the core level shift origin of sulfur and thiolates on Pd (111) surfaces. *Physical Chemistry Chemical Physics*, 17(37):24349–24355, 2015.

[108] Christian Kunkel, Francesc Vines, Pedro J Ramirez, Jose A Rodriguez, and Francesc Illas. Combining theory and experiment for multitechnique characterization of activated CO_2 on transition metal carbide (001) surfaces. *The Journal of Physical Chemistry C*, 123(13):7567–7576, 2018.

[109] Fabien Silly, Adam Q Shaw, Martin R Castell, GAD Briggs, Manuela Mura, Natalia Martsinovich, and Lev Kantorovich. Melamine structures on the Au (111) surface. *The Journal of Physical Chemistry C*, 112(30):11476–11480, 2008.

[110] H Ågren, J Müller, and J Nordgren. Vibrational excitations in soft x-ray emission and core ESCA spectra of NH_3. *The Journal of Chemical Physics*, 72(7):4078–4083, 1980.

[111] Sandra García-Gil, Andrés Arnau, and Aran Garcia-Lekue. Exploring large O 1s and N 1s core level shifts due to intermolecular hydrogen bond formation in organic molecules. *Surface Science*, 613:102–107, 2013.

[112] Dmitry Lebedev, Yuliana Pineda-Galvan, Yuki Tokimaru, Alexey Fedorov, Nicolas Kaeffer, Christophe Coperet, and Yulia Pushkar. The key RuV=O intermediate of site-isolated mononuclear water oxidation catalyst detected by in situ X-ray absorption spectroscopy. *Journal of the American Chemical Society*, 140(1):451–458, 2018.

[113] Henrique Musseli Cezar, Sylvio Canuto, and Kaline Coutinho. DICE: A Monte Carlo code for molecular simulation including Configurational Bias Monte Carlo method. *Journal of Chemical Information and Modeling*, 2020.

[114] Herbert C Georg, Kaline Coutinho, and Sylvio Canuto. Solvent effects on the UV-visible absorption spectrum of benzophenone in water: A combined Monte Carlo quantum mechanics study including solute polarization. *The Journal of Chemical Physics*, 126(3):034507, 2007.

[115] W Tang, E Sanville, and G Henkelman. A grid-based Bader analysis algorithm without lattice bias. *Journal of Physics: Condensed Matter*, 21(8):084204, 2009.

[116] David J Morgan. Resolving ruthenium: XPS studies of common ruthenium materials. *Surface and Interface Analysis*, 47(11):1072–1079, 2015.

[117] Robert O Jones. Density functional theory: Its origins, rise to prominence, and future. *Reviews of modern physics*, 87(3):897, 2015.

[118] Tangui Le Bahers, Michel Rerat, and Philippe Sautet. Semiconductors used in photovoltaic and photocatalytic devices: assessing fundamental properties from DFT. *The Journal of Physical Chemistry C*, 118(12):5997–6008, 2014.

[119] Shuning Xiao, Peijue Liu, Wei Zhu, Guisheng Li, Dieqing Zhang, and Hexing Li. Copper nanowires: a substitute for noble metals to enhance photocatalytic H_2 generation. *Nano letters*, 15(8):4853–4858, 2015.

[120] Qi Ding, Bo Song, Ping Xu, and Song Jin. Efficient electrocatalytic and photoelectrochemical hydrogen generation using MoS_2 and related compounds. *Chem*, 1(5):699–726, 2016.

[121] Thomas F Jaramillo, Kristina P Jørgensen, Jacob Bonde, Jane H Nielsen, Sebastian Horch, and Ib Chorkendorff. Identification of active edge sites for electrochemical H_2 evolution from MoS_2 nanocatalysts. *science*, 317(5834):100–102, 2007.

[122] Joohee Lee, Sungwoo Kang, Kanghoon Yim, Kye Yeop Kim, Ho Won Jang, Youngho Kang, and Seungwu Han. Hydrogen evolution reaction at anion vacancy of two-dimensional transition-metal dichalcogenides: ab initio computational screening. *The Journal of Physical Chemistry Letters*, 9(8):2049–2055, 2018.

[123] Dequan Er, Han Ye, Nathan C Frey, Hemant Kumar, Jun Lou, and Vivek B Shenoy. Prediction of enhanced catalytic activity for hydrogen evolution reaction in Janus transition metal dichalcogenides. *Nano letters*, 18(6):3943–3949, 2018.

[124] Jinsong Wang, Jia Liu, Bao Zhang, Xiao Ji, Kui Xu, Chi Chen, Ling Miao, and Jianjun Jiang. The mechanism of hydrogen adsorption on transition metal dichalcogenides as hydrogen evolution reaction catalyst. *Physical Chemistry Chemical Physics*, 19(15):10125–10132, 2017.

[125] Berit Hinnemann, Poul Georg Moses, Jacob Bonde, Kristina P Jørgensen, Jane H Nielsen, Sebastian Horch, Ib Chorkendorff, and Jens K Nørskov. Biomimetic hydrogen evolution: MoS_2 nanoparticles as catalyst for hydrogen evolution. *Journal of the American Chemical Society*, 127(15):5308–5309, 2005.

[126] Yun Zheng, Lihua Lin, Bo Wang, and Xinchen Wang. Graphitic carbon nitride polymers toward sustainable photoredox catalysis. *Angewandte Chemie*

International Edition, 54(44):12868–12884, 2015.

[127] Jens Kehlet Nørskov, Thomas Bligaard, Ashildur Logadottir, JR Kitchin, Jingguang G Chen, S Pandelov, and U Stimming. Trends in the exchange current for hydrogen evolution. *Journal of The Electrochemical Society*, 152(3):J23, 2005.

[128] Walter Kohn and Lu Jeu Sham. Self-consistent equations including exchange and correlation effects. *Physical Review*, 140(4A):A1133, 1965.

[129] Georg Kresse and Jürgen Hafner. Ab initio molecular dynamics for liquid metals. *Physical Review B*, 47(1):558, 1993.

[130] Georg Kresse and Jürgen Furthmüller. Efficient iterative schemes for ab initio total-energy calculations using a plane-wave basis set. *Physical review B*, 54(16):11169, 1996.

[131] Georg Kresse and Jürgen Furthmüller. Efficiency of ab-initio total energy calculations for metals and semiconductors using a plane-wave basis set. *Computational Materials Science*, 6(1):15–50, 1996.

[132] James D Pack and Hendrik J Monkhorst. Special points for brillouin-zone integrations - a reply. *Physical Review B*, 16(4):1748, 1977.

[133] Xinguo Ma, Chen Chen, Jisong Hu, Mingkun Zheng, Huihu Wang, Shijie Dong, Chuyun Huang, and Xiaobo Chen. Evidence of direct Z-scheme g-C_3N_4/WS_2 nanocomposite under interfacial coupling: First-principles study. *Journal of Alloys and Compounds*, 788:1–9, 2019.

[134] Xinguo Ma, Jisong Hu, Hua He, Shijie Dong, Chuyun Huang, and Xiaobo Chen. New understanding on enhanced photocatalytic activity of g-C_3N_4/$BiPO_4$ heterojunctions by effective interfacial coupling. *ACS Applied Nano Materials*, 1(10):5507–5515, 2018.

[135] Peter E Blöchl, Ove Jepsen, and Ole Krogh Andersen. Improved tetrahedron method for Brillouin-zone integrations. *Physical Review B*, 49(23):16223, 1994.

[136] Georg Kresse and Jürgen Furthmüller. Efficient iterative schemes for ab initio total-energy calculations using a plane-wave basis set. *Physical Review B*, 54(16):11169, 1996.

[137] RW Ramette. Outmoded terminology: The normal hydrogen electrode. *Journal of Chemical Education*, 64(10):885, 1987.

Acta Universitatis Upsaliensis

*Digital Comprehensive Summaries of Uppsala Dissertations
from the Faculty of Science and Technology* 1954

Editor: The Dean of the Faculty of Science and Technology